

THESIS FOR THE DEGREE OF LICENTIATE OF ENGINEERING

# Single Copper Nanoparticle Oxidation

Studied by Correlative Optical and Electron Microscopy

SARA NILSSON



Department of Physics

CHALMERS UNIVERSITY OF TECHNOLOGY

Gothenburg, Sweden 2019

Single Copper Nanoparticle Oxidation  
Studied by Correlative Optical and Electron Microscopy  
SARA NILSSON

© SARA NILSSON, 2019.

Department of Physics  
Chalmers University of Technology  
SE-412 96 Gothenburg  
Sweden  
Telephone + 46 (0)31-772 1000

Cover:  
The scrutiny of single copper nanoparticles during oxidation symbolized by the magnifying glass. Artist: Erik Larsson.

Printed at Chalmers Digitaltryck  
Gothenburg, Sweden 2019

Single Copper Nanoparticle Oxidation  
Studied by Correlative Optical and Electron Microscopy

Sara Nilsson  
Department of Physics  
Chalmers University of Technology

## Abstract

Cu nanoparticles are commonly used in microelectronic devices and as catalysts in, for example, methanol synthesis and methanol steam reforming reactions. However, Cu nanoparticles are prone to oxidation. During the oxidation process, so-called Kirkendall voids often form due to different diffusion rates of oxygen and copper ions through the growing oxide. The growing void transforms the nanoparticle structure, which may lead to fatal failure of microelectronic devices or to radically different catalytic properties. It is therefore of interest to gain deeper insight into the oxidation mechanism of nanoparticles to, for instance, understand under which conditions Kirkendall voids form. As there is evidence that the grain structure significantly affects the oxidation mechanism and may accelerate or suppress the Kirkendall void formation, it is desirable to study the oxidation of Cu nanoparticles at the single particle level under close-to real application conditions

In this thesis, I have developed an *in situ* experimental method for studying the oxidation of single Cu nanoparticles. It combines the structural information from TEM imaging with a non-invasive optical dark-field scattering spectroscopy method – plasmonic nanospectroscopy – that enables the tracking of oxidation kinetics in real time. In this way, I can minimize exposure of the particles to the electron beam in the TEM, and, thus, minimize the risk for beam-induced structural and chemical changes to the particles during the experiments.

Using this platform in combination with finite-difference time-domain electrodynamic simulations, I was able to systematically analyze the single particle optical response measured in the experiments and, thus, shed light on the oxidation of the single Cu nanoparticles from a mechanistic perspective. As the first key result, we found a distinct evolution of the single particle dark-field scattering spectra of single Cu nanoparticles, which is indicative of Kirkendall void formation. As the second key result, we identified a clear dependence of the induction time to the onset of Kirkendall void formation on the grain structure of the single nanoparticles.

**Keywords:** oxidation, nanoscale Kirkendall effect, single particle, plasmonic sensing, dark-field scattering spectroscopy, transmission electron microscopy, plasmonic nanospectroscopy



# LIST OF APPENDED PAPERS

The thesis is based on the work presented in the following papers:

## **PAPER I**

### ***In Situ* Plasmonic Nanospectroscopy of Single Cu Nanoparticle Oxidation and Kirkendall Void Formation**

Sara Nilsson, David Albinsson, Tomasz J. Antosiewicz, Joachim Fritzsche and Christoph Langhammer

*Submitted*

## **PAPER II**

### **Grain Boundary Mediated Oxidation of Single Cu Nanoparticles**

Sara Nilsson, David Albinsson, Alice Bastos da Silva Fanta, Joachim Fritzsche and Christoph Langhammer

*In Manuscript*

## RELATED PAPERS NOT INCLUDED IN THE THESIS

### **Heterodimers for *in Situ* Plasmonic Spectroscopy: Cu Nanoparticle Oxidation Kinetics, Kirkendall Effect and Compensation in the Arrhenius Parameters**

David Albinsson, Sara Nilsson, Tomasz J. Antosiewicz, Vladimir P. Zhdanov and Christoph Langhammer

*J. Phys. Chem. C*, **123**, 10 (2019)

### **A Nanofluidic Device for Parallel Single Nanoparticle Catalysis in Solution**

Sune Levin, Joachim Fritzsche, Sara Nilsson, Bhausaheb Dhokale, August Runemark, Henrik Ström, Henrik Sundén, Christoph Langhammer and Fredrik Westerlund

*Under revision*

### **A Fiber-Optic Nanoplasmonic Hydrogen Sensor *via* Pattern-Transfer of Nanofabricated PdAu Alloy Nanostructures**

Ferry A. A. Nugroho, Robin Eklund, Sara Nilsson and Christoph Langhammer

*Nanoscale*, **10**, 44 (2018)

## MY CONTRIBUTION TO THE APPENDED PAPERS

**Paper I:** Performing all the correlative optical and electron microscopy measurements, FDTD simulations apart from building the geometry, data analysis and figure preparation, writing the first draft of the paper.

**Paper II:** Performing all the correlative optical and electron microscopy measurements, data analysis and figure preparation and writing parts of the first draft of the paper.

# CONTENT

<b>1</b>	<b>INTRODUCTION.....</b>	<b>1</b>
1.1	<i>WHY AND HOW TO STUDY SINGLE NANOPARTICLES .....</i>	2
1.2	<i>IN SITU OXIDATION BY LSPR.....</i>	3
1.3	<i>IN SITU OXIDATION BY ENVIRONMENTAL TEM.....</i>	4
1.4	<i>THE SCOPE OF THIS THESIS .....</i>	4
1.5	<i>THE OUTLINE OF THIS THESIS .....</i>	5
<b>2</b>	<b>OXIDATION OF METALS.....</b>	<b>7</b>
2.1	<i>OXIDATION OF METAL SURFACES .....</i>	7
2.2	<i>OXIDATION OF METALS AT THE NANOSCALE.....</i>	10
2.2.1	<i>A general model for oxidation of spherical particles.....</i>	12
2.2.2	<i>Suppressing void formation upon Cu oxidation.....</i>	14
<b>3</b>	<b>NANOPLASMONICS.....</b>	<b>17</b>
3.1	<i>ELECTRONS IN METALS .....</i>	18
3.2	<i>THE QUASI-STATIC APPROXIMATION.....</i>	19
3.3	<i>PARTICLE SHAPE EFFECTS .....</i>	22
3.4	<i>LSPR SENSING.....</i>	23
3.5	<i>SINGLE NANOPARTICLE PLASMONICS .....</i>	25
<b>4</b>	<b>NANOFABRICATION.....</b>	<b>27</b>
4.1	<i>LITHOGRAPHY .....</i>	27
4.1.1	<i>Colloidal lithography.....</i>	28
4.1.2	<i>Hole-mask colloidal lithography.....</i>	28
4.1.3	<i>Electron-beam lithography.....</i>	29
4.2	<i>SPIN-COATING.....</i>	30
4.3	<i>ETCHING.....</i>	30

4.4 THIN FILM DEPOSITION .....	31
<b>5 MICROSCOPY.....</b>	<b>33</b>
5.1 DARK-FIELD SCATTERING SPECTROSCOPY .....	34
5.2 TRANSMISSION ELECTRON MICROSCOPY .....	36
5.3 SCANNING ELECTRON MICROSCOPY.....	38
5.4 ATOMIC FORCE MICROSCOPY .....	38
<b>6 A CORRELATIVE DFSS AND TEM METHOD .....</b>	<b>41</b>
6.1 INITIAL ANNEALING.....	41
6.2 PRE-OXIDATION TEM IMAGING.....	42
6.3 DFSS IN SITU OXIDATION MEASUREMENT.....	43
6.4 POST-OXIDATION TEM IMAGING .....	45
6.5 DATA ANALYSIS.....	45
<b>7 SUMMARY AND OUTLOOK.....</b>	<b>47</b>
7.1 SUMMARY OF THE APPENDED PAPERS .....	47
7.2 OUTLOOK .....	48
<b>ACKNOWLEDGEMENTS .....</b>	<b>51</b>
<b>BIBLIOGRAPHY .....</b>	<b>53</b>

# 1 INTRODUCTION

There is an increasing awareness for the limited amount of our natural resources, which naturally should induce a driving force for protecting things we produce out of these materials to make them last as long as possible. From this point of view, it is necessary to map the conditions under which materials deteriorate, for example when metals corrode or wood rots. Through history, humans have invented solutions for how to protect materials from one of its most abundant enemies – water – for example by mixing metals into stainless alloys to keep them from corroding and by painting wood to keep moisture out.

Since we in recent years have tremendously decreased the length scales at which we engineer materials we use in new technologies, there is an increased need to understand corrosion and wear of these smaller structures, known as *nanomaterials*. In this introductory chapter, I will make an attempt at motivating the study of corrosion of nanomaterials, on a single nanoparticle-level, and in particular why it is interesting to study the oxidation of copper nanoparticles. Furthermore, I will also motivate the method I have used to perform this study.

One among the various applications of nanoparticles is found in catalysis. Cu nanoparticles are active catalysts for a number of important chemical processes, such as methanol synthesis from  $H_2$  and  $CO_2$  and methanol steam reforming to produce hydrogen.<sup>1</sup> Using the first process one can make use of sequestered  $CO_2$  to produce methanol, which is a promising candidate for storing electrical energy in a chemical form, as discussed in terms of a methanol economy.<sup>2</sup> Furthermore, the hydrogenation of CO and  $CO_2$  into hydrocarbons is commonly known as the Fischer-Tropsch process, however, traditionally fossil carbon sources, such as crude oil, are used as a source for CO and  $CO_2$ .<sup>3</sup> In light of the recent advancements in sequestration of  $CO_2$ , collected exhaust  $CO_2$  has become a possible source for  $CO_2$  in methanol synthesis providing a more sustainable raw material.<sup>2,4</sup> However, to increase Cu catalyst efficiency, for example in methanol synthesis, and prolong its lifetime, we need to gain better understanding for how it oxidizes.

Apart from its applicability in catalysis, Cu is also widely used in microelectronics where it is a favorable conductor due to its low resistivity. However, when Cu is oxidized these properties are lost, resulting in breakdown of the microelectronic circuit.<sup>5</sup> Hence, also in

this context, fundamental understanding of the copper nanostructure oxidation is of importance.

## 1.1 Why and how to study single nanoparticles

Why bother studying one *tiny* metal piece, such as a nanoparticle? One thousand times smaller in size than the diameter of a single strand of hair, which is already on the limit of what our eyes can resolve. So how can one study something that is one thousand times smaller than a single hair? To get a perspective on how large one thousand times is; imagine you run to catch the bus, it might be a distance of around 42 meters, which you might find not too exhausting. Then imagine you run one thousand times longer, which is 42 000 meters, the approximate length of a full marathon. This would be a challenge on another scale, another length scale that is. In science, one often refers to different scales for comparing things. Our daily life takes place in the macroscopic world, or on the macroscopic scale. This includes things we can see and experience with our senses. However, there are things that take place on larger or smaller, and faster or slower scales than what we can appreciate. For example, the speed of light is much faster than what we can comprehend. Despite this, we can make use of it to achieve fast communication via optical fibers that transmit light signals from one end to another, providing us with fast internet connection and the possibility to communicate all over the world in one instant.

In a similar way, nanostructures provide us with technologies that improve our life even though we cannot use our senses to detect or probe them. Hence, we need to make use of other instruments to study them, which work on that particular length scale referred to as the *nanoscale*. For this purpose energies and distances on a similar scale are required. For example, we can use electrons that when accelerated to energies of 100 keV have wavelengths of a few picometers<sup>6</sup> (one thousand times smaller again than a nanometer). This, on the other hand, seems too short for nanoscale resolution, but due to imperfect lenses picometer resolution is not achieved. Hence, it is appropriate for resolving nanostructures. In a similar manner, photons can be found with wavelengths spanning several length scales, from radio waves with wavelengths of several meters, which require antennas on the same length scale, down to X-rays with wavelengths comparable to the size of an atom. Nanoparticles also act as antennas for photons, which at the optical wavelengths (450-700 nm) that our eyes can detect is called light. Even though the optical wavelengths of the photons are longer than the size of the nanoparticles, the photons can still interact with the nanoparticles. Since they, when interacting with light, appear to be larger than what they actually are, due to the electrons of the metal interacting with the photons. I will go deeper into the interaction between metals and light, and particularly metal nanostructures in chapter 3.

Back to the original question, but let us now emphasize another word: Why bother studying *one* tiny metal piece? It is possible to study millions of small nanoparticles as an ensemble and get out the average response of those. Why isn't that enough? If you imagine a group of people, for example travelling on a bus in the morning, they all will be pretty much the same in the sense that all are humans. They have a lot of common attributes such as hands, feet, arms, legs, eyes etc. But if you look more closely they will

all be a bit different, and not to mention their abilities and personal characters. Even though the basic abilities are the same of most people, there is an infinite spectrum of individual personalities, some may be more artistic and creative, others are better at analyzing facts and some are more prone to care for other people etc. This is something you do not notice at a first glance. The same is true for nanoparticles, they may not be as complex and versified as human beings, but still there are a lot of properties which cannot be seen when averaging over a large group. Hence, one has to study them one by one and get to know each individual to learn more about its particular characteristics and behavior. Applied to the oxidation of nanoparticles, and in particular those made of Cu which my work concerns, properties such as their size and shape, as well as their *grain structure*, which refers to how they are built up out of smaller crystal pieces known as crystal grains, will affect the oxidation mechanism. These are things we can only learn by studying them one by one, as they are not all exactly the same.

## 1.2 *In Situ* oxidation by LSPR

The plasmonic response of a nanoparticle, also referred to as the localized surface plasmon resonance (LSPR), is widely used for sensing in biophysics<sup>7</sup> and has recently emerged as a powerful sensing approach within gas sensing<sup>8</sup> and materials research<sup>9</sup>. Some of the esteemed properties of LSPR sensing and the reasons for the widening of its applications, is the fast response rate, small amount of required sample material, easy readout in the far field of either the transmitted or scattered light, and compatibility with fabricating a fiber optical sensor<sup>10</sup>. Thanks to these properties and that Cu in its metallic state is an efficient plasmonic material with its resonance in the visible region of the spectrum, it is also viable to use LSPR sensing to study the oxidation of Cu nanoparticles. As Cu oxidizes, the plasmonic resonance undergoes drastic changes, initial red-shift due the sensitivity of the plasmonic resonance for an increase in the refractive index of the surrounding medium, followed by a decrease due to the shrinking metal volume and finally, the resonance vanishes completely upon full oxidation. Due to this clear response, there are several successful reports where LSPR is used<sup>11–13</sup>. Among these, one was conducted by David Albinsson et al<sup>11</sup> in our group, where he used a second plasmonic antenna of gold (Au) next to the smaller Cu nanoparticle to detect a readout even after full oxidation of the Cu nanoparticle. However, so far there is only one report that I know of concerning the probing of single Cu nanoparticle oxidation by LSPR<sup>14</sup>, however, not focusing on the oxidation mechanism as such and the rest have been on an ensemble level. Thus they are not providing any insights in the dependence of the oxidation mechanism on the particle specific properties such as size, shape and grain structure.

LSPR sensing on the single-nanoparticle-level, can be realized by dark-field scattering spectroscopy (DFSS), where the scattered light from single nanoparticles is detected, as visualized in Figure 1.1A. Finally, I think it is also worth mentioning the main weakness of LSPR sensing, namely that it is non-specific. In other words, *any* change in or around the nanoparticle may induce a response in the readout. Therefore, it is required to use complementary methods to corroborate that the response is indeed due to the process of interest, like oxidation in the present case.

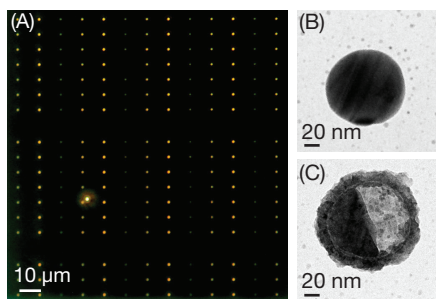


Figure 1.1: Presenting the DFSS and TEM methods and their respective length scales. (A) A photograph taken by means of optical dark-field microscopy, where columns of Cu nanoparticles separated by  $10\ \mu\text{m}$  appear as bright spots. Before (B) and after (C) an *in situ* oxidation measurement, a Cu nanoparticle's grain structure is captured by TEM. Note the scale bar of 20 nm. TEM allows to capture the nanoparticles on another length scale compared to DFSS. In (C) the Kirkendall void forming during oxidation of a Cu nanoparticle is clearly visible, here it covers half of the core of the nanoparticle.

### 1.3 *In Situ* oxidation by environmental TEM

A second viable method for studying oxidation of Cu nanoparticles is environmental, or *in situ*, transmission electron microscopy (TEM). This is a powerful method that enables imaging of the nanoparticles during the oxidation reaction. TEM on its own provides a means for studying oxidation mechanisms on the single particle level, as demonstrated last year in the report by Huang et al<sup>15</sup>, where the authors show that the type of grain boundary dictates if a Kirkendall void is forming or not. However, so far there are only a handful of studies on Cu oxidation by *in situ* TEM<sup>16–18</sup>. Perhaps the reason is that the oxidation kinetics might be affected by the high energy beam<sup>19</sup>, as well as it is an expensive technique with high operational complexity. In recent years, reactions under atmospheric pressures are realized<sup>18</sup>, however, it further complicates the process by means of sample assembly and gas infrastructure. With this in mind, combining TEM with a less invasive and less complex method such as DFSS, as presented in Figure 1.1, that still allows for following the oxidation of single nanoparticles *in situ* at atmospheric pressures might be the way to go.

### 1.4 The scope of this thesis

My aim when writing this thesis is to condense some of the theories and concepts describing this particular research field presented here into something that can, hopefully, be understandable to various people of different backgrounds and not only those already experts in the field. You as a reader might not find all parts equally interesting. In that case you are welcome to skip those parts. Along the way, I have tried to include examples of how I understand and interpret concepts, and relate those to our everyday life, as this is how I like to envision science.

In the longer term, the goal of my work is to develop a combined DFSS-TEM method that can be used for mechanistic studies on single nanoparticles to gain fundamental

insights into questions related to materials research and catalysis. The method provides a more gentle path for *in situ* studies compared to environmental TEM, however, the challenges lie in the non-specificity of the LSPR readout.

In the work presented here, a few steps in that direction are taken. In **paper I**, the method of studying oxidation of single Cu nanoparticles by means of dark-field scattering spectroscopy (DFSS) combined with TEM is introduced. This method enables us to follow the optical scattering response of individual nanoparticles *in situ* at atmospheric pressures during the oxidation reaction. The evolution of the collected scattering spectra during the oxidation was at first quite remarkable and surprising. In previously reported ensemble studies of Cu nanoparticle oxidation, the plasmonic resonance first showed a red-shift followed by a decrease in intensity, as described above. We did observe these changes, as well as a split of the resonance peak into two modes in the majority of the studied nanoparticles, which could not be resolved in the ensemble studies. By building a model for finite-difference time-domain (FDTD) simulations, we could validate our hypothesis of the fundamental origin of the peak split being the onset of so-called Kirkendall void formation.

In **paper II**, results obtained by the combined DFSS-TEM method established for studying the oxidation of Cu nanoparticles *in situ* by correlating the LSPR readout with the particle grain structure pre- and post-oxidation, were further scrutinized to extract some relation between the grain structure and oxidation kinetics.

## 1.5 The outline of this thesis

The first two chapters following this introductory one are of a theoretical character, where I explain some models that describe the mechanisms observed when studying the oxidation of metals (**chapter 2**) and the interaction of metals and light (**chapter 3**). In **chapter 4**, an introduction to the used nanofabrication techniques is given, that is, hole-mask colloidal lithography and electron beam lithography. In **chapter 5**, the basic principles of optical dark-field scattering spectroscopy and transmission electron microscopy are summarized, which in **chapter 6** are combined to the correlative DFSS-TEM method that I have developed in this thesis. Finally, in **chapter 7**, a summary of the appended papers, as well as an outlook for future work is given.



## 2 OXIDATION OF METALS

We recognize corrosion of metals from everyday life in rusty cars and green copper roofs. Oxidation of iron might be the most well-known type of corrosion, widely referred to as rust. However, chemically, rust is known as hematite ( $\text{Fe}_2\text{O}_3$ ).<sup>20</sup> When the corrosion of iron has proceeded long enough, the rust will eventually consume all the iron and result in a porous oxide material. However, Cu does not disintegrate upon oxidation, but rather forms a self-limiting oxide film on the surface, protecting the bulk from further corrosion.

As Cu is the main character of this thesis, it will be in the spotlight in this chapter, when the oxidation of metals is introduced. Cu is commonly associated with a dark orange color but surprisingly, this is not the color of Cu but of one of its oxide forms, namely  $\text{Cu}_2\text{O}$ . The actual color of pure Cu is brightly pink, but it is very rarely seen because in air Cu is rapidly covered with a thin layer of  $\text{Cu}_2\text{O}$ .<sup>21</sup> As mentioned above, green roof plates are also often associated with Cu. The green color, comes from copper salts that form when Cu reacts with molecules from the atmosphere, mainly containing S, but also Cl or C.<sup>21,22</sup>

To better understand the oxidation of Cu at the nanoscale is of interest thanks to its catalytic properties<sup>23</sup>, as well as its excellent electronic conduction<sup>24</sup>. Cu is an active catalyst for methanol synthesis and methanol steam reform reactions.<sup>1</sup> Cu is also the most commonly used metal for electronic conduction, as it has low resistivity and high thermal conductivity.<sup>24</sup> Hence, it is important to map the oxidation conditions for Cu to keep it in its metallic form, in order to preserve conduction properties or understanding which oxide state is prevalent during catalysis.

In this chapter, some general theories for oxidation of bulk metals will be introduced, as well as some models concerning the oxidation of nanomaterials. As most of the models for oxidation on the nanoscale have emerged from the macroscopic models, our discussion will start there.

### 2.1 Oxidation of metal surfaces

From a chemical point of view, oxidation is simply removing electrons from an atom or a molecule. For the ease of the discussion, we will restrict ourselves to metals. In this

context one often talks about the different oxidation states of metals. Removing one electron from a metal atom yields a metal ion  $M^+$ , which is in the first oxidation state  $M(I)$ . Further removing one electron yields  $M(II)$ . For the example of copper, the first and second oxidation state are the most frequently occurring, called  $Cu(I)$  and  $Cu(II)$  (spelled out as “copper one” and “copper two”) and the corresponding oxides are  $Cu_2O$  for  $Cu(I)$  and the  $Cu(II)$  oxide is  $CuO$ .  $Cu_2O$  is also known as *cuprous oxide* and  $CuO$  as *cupric oxide*.<sup>22</sup>

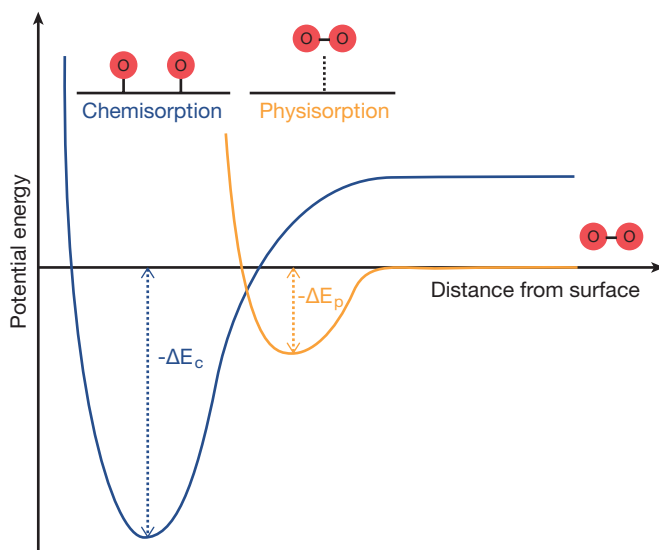


Figure 2.1: The Lennard-Jones potential. The interaction between the surface and a gas molecule is at relatively large distances described by the Lennard-Jones potential. The gas molecule is attracted by the physical van der Waals force resulting in physisorption. By interaction with the electronic orbitals of the metal surface, the molecule can be chemically bonded, also known as chemisorption.

Now, when the formalities are settled, we can start looking into the physics and chemistry explaining the oxidation of metal surfaces. The first step of oxidation is adsorption of oxygen on the surface. Molecules can either be physically adsorbed without breaking the molecular bond, or chemisorbed by forming a chemical bond, as depicted in Figure 2.1.<sup>25</sup> When a gas molecule comes close enough to the surface, it is attracted by the physical van der Waals force and stays at a distance equal to the sum of the van der Waals radii of the surfaces atom and the gas atom, which is on the order of a few Ångström.<sup>25</sup> In gas phase, the oxygen molecule is unlikely to overcome the barrier of the dissociation energy 500 kJ/mol<sup>26</sup>. However, when physisorbed on the surface of a transition metal, the energy barrier for chemisorption is usually lower than for desorption from the surface, hence it is likely that the molecular bond is broken and each atom becomes chemically bonded to a surface atom. There are also cases of associative chemisorption, as for  $CO$ , which has a very strong molecular bond and thus the molecule can form a chemical bond to the metal surface.<sup>27</sup> As more and more atoms are adsorbed to the surface, the gain in energy for chemisorption will be less leading to a saturation coverage.<sup>25</sup>

When oxygen is adsorbed to the surface, it needs to diffuse into the metal to form the oxide. To accommodate the oxygen atoms in the metal, vacancies in the metal lattice are required or that oxygen atoms are allowed to occupy interstitial sites in the lattice. Commonly, metals do have lattice defects, particularly at elevated temperatures.<sup>28</sup> However, there exist other pathways for diffusion in metals and metal alloys. Two atoms can change positions in the lattice, commonly referred to as *position interchange*, or four atoms next to each other in a ring can change positions, known as *ring diffusion*.<sup>28</sup> For this diffusion path, no lattice defects are required. However, if the diffusion rates of two metals are different, mass will be transported in one direction across the diffusion interface. This was experimentally shown for the first time by Smigelskas and Kirkendall.<sup>28</sup> They studied the diffusion in a copper-plated brass volume and noted that more Zn was diffusing outwards from the brass than Cu was diffusing into the brass volume, due to the higher diffusion rate of Zn compared to Cu. This is now referred to as the Kirkendall effect.<sup>28</sup> At a Cu-Ni interface on the other hand, more Cu atoms diffuse into Ni, yielding a net mass diffusion across the interface. In the ideal Kirkendall effect the interface is shifting, however, if the interface is static, the net mass transport will lead to vacancies on the Cu-side and a swelling on the Ni-side of the interface.<sup>28</sup>

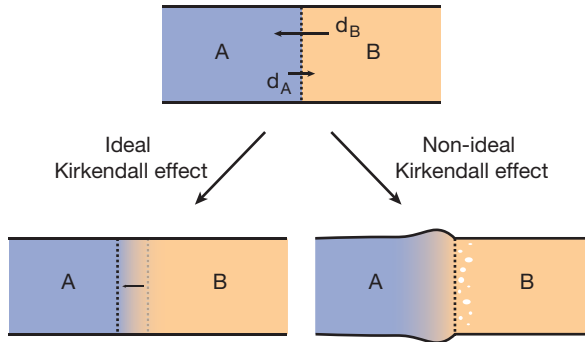


Figure 2.2: The Kirkendall effect. The two cases, ideal and non-ideal Kirkendall effect, are schematically depicted. In the ideal Kirkendall effect, the interface is shifted, which applies to the case of Cu (material A) and brass (Zn is material B). The non-ideal case applies to Ni (material A) - Cu (material B) interfaces, where voids form on the Cu-side of the interface.

Diffusion of metal ions in the metal itself is referred to as *self-diffusion*. At moderately high temperature ( $>200^{\circ}\text{C}$ ), vacancy diffusion is the predominant factor for self-diffusion in Cu, while at lower temperatures ( $<100^{\circ}\text{C}$ ) interstitial diffusion is dominating. The activation energy for self-diffusion in Cu is 2.1 eV.<sup>28</sup> Theoretically, the net transport of atoms between two lattice planes can be described as

$$\frac{dn_A}{dt} = -k_A n_v a^2 \frac{dn_A}{dx} \quad (2.1)$$

where  $n_A$  and  $n_v$  are the concentrations of atoms and vacancies, respectively,  $k_A$  is the diffusion rate constant of metal A and  $a$  is the distance between the planes.<sup>28</sup> As  $dn_A/dx$  is the concentration gradient of A, we see that the net transport is in the opposite

direction. Here, the diffusion coefficient is defined as  $D = k_A n_v a^2$ . However, in polycrystalline metals, grain boundary diffusion dominates over lattice diffusion below some critical temperature at which the diffusion rates are equal. The critical temperature depends on properties of the specific material at hand, such as crystal structure, grain boundary density and stress at the grain boundary due to lattice deformation.<sup>28</sup>

Comparing the oxidation rates of Cu and Al gives a good example for demonstrating the importance of vacancy density on the oxidations rates. The free energy of formation of the oxides at 600°C are  $\Delta H_{Al_2O_3} = -220$  kcal/mol and  $\Delta H_{Cu_2O} = -55$  kcal/mol,<sup>28</sup> which tells us that more energy is gained by forming the aluminum oxide. The lattice defect concentration is much higher in Cu<sub>2</sub>O compared to Al<sub>2</sub>O<sub>3</sub> at high temperatures, resulting in a much higher oxidation rate of Cu due to the many paths for ions to diffuse through the oxide layer to the metal/oxide interface.

At room temperature, some metals such as Al, quickly form a thin oxide of only a few atomic layers. At low temperatures, the oxidation is driven by an electric field over the oxide rather than by temperature, this is known as the Cabrera-Mott model.<sup>29</sup> The field originates from the potential between metal cations at the metal/oxide interface and oxygen anions at the oxide/gas interface, assuming that electrons move through the oxide film much faster than the ions. The strength of the field is  $F = V/d$ , where  $V$  is the potential from the ions and  $d$  is the thickness of the field. The field is only strong enough to drive oxidation for thin oxide films,  $d > 100$  Å. Hence, after reaching a critical thickness, oxidation will stop. At low temperatures, the thickness of the oxide film is limited by the misfit between the oxide and the metal lattice. If the misfit is large (>15%), the oxide will keep its natural lattice parameter and will keep on growing. However, if the lattice misfit is smaller, the oxide will rearrange its lattice to fit the metal and after a few layers of oxide the strain will be too large and oxidation will stop.<sup>29</sup> However, this is only valid in the low temperature limit. At higher temperatures, the oxide can recrystallize into its natural lattice parameter.

My aim of this chapter was to give a short introduction to some concepts governing the oxidation of metal surfaces. We have touched upon some of the steps during oxidation, such as oxygen adsorption and bond breaking, the diffusion of metal ions and vacancies, which, for systems of different diffusion rates, can be described by the Kirkendall effect, as well as by the Cabrera-Mott model describing oxidation driven by the potential field in the oxide. However, numerous models exist that I have chosen not to include in this introduction to the subject. For the interested reader, I strongly recommend the book by Hauffe<sup>28</sup>, which provides a comprehensive description of the field.

## 2.2 Oxidation of metals at the nanoscale

As we shrink metals down to the nanoscale, most of the concepts and theories introduced in last section will still be valid, as well as some new models will be introduced to deal with geometries of nanomaterials. On a macroscopic scale, the surface/volume ratio is approaching zero as the bulk is assumed to extend into infinity. However, on the nanoscale, the surface/volume ratio is much larger and will affect the oxidation

mechanisms. Oxidation of bulk metals is in many cases limited to the surface but due to the large surface/volume ratio of nanomaterials, the geometry may change completely upon oxidation, as we will see some examples of in this section.

At the nanoscale, the dominating oxidation mechanism not only determines the rate of oxidation, but also the end geometry. As various mechanisms and end geometries have been reported, there are a multitude of models explaining the effects of these different mechanisms. One of the most common is the nanoscale Kirkendall effect (NKE) derived from the macroscopic Kirkendall effect, depicted in Figure 2.3A. At the nanoscale, NKE is mainly referring to, as far as I know, cases where one or several voids form in the center of the nanomaterial. Hence, it originates from the non-ideal Kirkendall effect, where small voids form at the interface due to a net transport of mass across the interface. Apart from NKE, the Cabrera-Mott (Figure 2.3C) model has also been shown to apply to nanoparticles. Fe particles at room temperature formed an oxide layer of 2.2 nm in one day, independent of particle size. After the initial oxide film had formed the continued oxidation was significantly slowed down, which was attributed to decreased field strength  $F$  as the oxide film grows, according to the Cabrera-Mott model.<sup>30</sup>

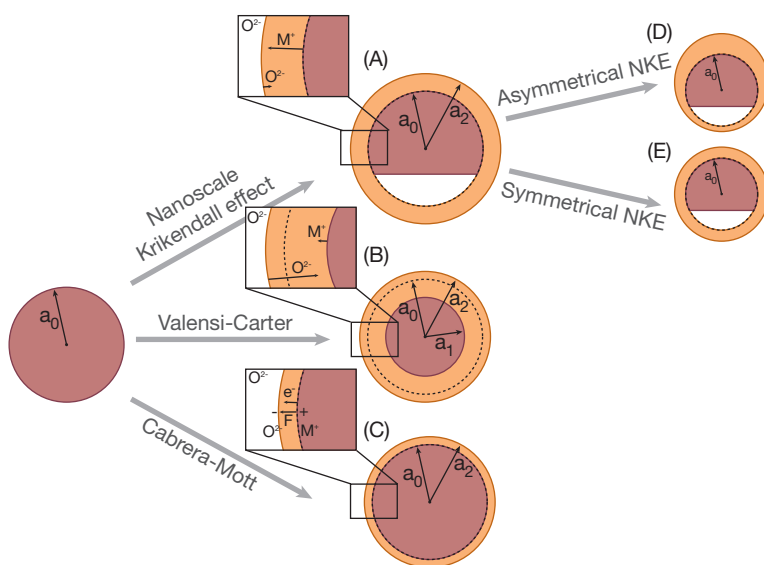


Figure 2.3: Schematic illustration of the pathways for nanoscale oxidation. (A) The nanoscale Kirkendall effect (NKE), recognized by the characteristic void inside the core due to net outward mass transport. The Kirkendall effect can result either in an inhomogeneous oxide shell (D) as in the case of Ni or a homogeneous oxide shell (E) as for Cu. (B) The Valensi-Carter model describing oxidation of a nanoparticle with net inward mass transport, no void is formed. (C) The Cabrera-Mott model, a thin oxide layer is formed at room temperature due to the driving potential field in the oxide.

In the opposite case of NKE, there is a net inward transport of mass, which is described by the Valensi-Carter model<sup>31,32</sup>, depicted in Figure 2.3B. In the case of a higher diffusion rate of  $O^{2-}$  through the oxide compared to  $M^+$ , the oxide formation will occur mainly at

the oxide/metal interface. There will be a net outward flow of vacancies, therefore, no void will form in the center and the oxide/metal interface will shift inwards as the metal core is shrinking in volume. This shift is commonly known as a *Kirkendall shift*.<sup>32</sup>

Depending on the difference in diffusion rates, but possibly also on other parameters such as grain structure and lattice defects, the end geometry of the NKE can vary in between materials and nanostructures. I have chosen to include two examples of different end results from NKE. After void nucleation at the metal/oxide interface, the sequential oxide growth can either yield a homogenous or an inhomogeneous shell (Figure 2.3D,E). The inhomogeneous oxide shell resulting from NKE has been shown for Ni nanoparticles of 26 nm diameter. In this case, the shell is evidently thicker on the side opposite of the initial void nucleation site due to minimal sideways diffusion of Ni ions at the metal/oxide interface or in the NiO.<sup>33</sup> Oxidation of Cu nanoparticles on the other hand, has been shown to result in homogeneously thick oxide shells. Furthermore, the oxide is polycrystalline, giving it the characteristically rough surface.<sup>12,34</sup> As well as to nanoparticles, the NKE also applies to nanowires, resulting in hollow nanotubes, which can be utilized for fabrication of nanotubes.<sup>35</sup> Apart from a void growing from one side to the other, there is at least one reported case demonstrating NKE on Co reacting with Se, where the remaining metallic core is suspended by thin bridges from the shell, along which ions are transported for further reaction. This also tells us that the Kirkendall effect does not solely apply to oxidation, but any reaction where there is a difference in diffusion rates. To this end, in addition to O, it has also been shown for reactions between nanoparticles of various metals and S, Se or P.<sup>30,36</sup> There are also other routes resulting in hollow nanoparticles, mainly explored within colloidal nanoparticle synthesis, such as galvanic replacement of metal cations or anion exchange.<sup>30</sup>

## 2.2.1 A general model for oxidation of spherical particles

The models introduced in the previous section are describing extreme cases, where the oxidation mechanism is assumed to be only O<sup>2-</sup> inwards diffusion or M<sup>+</sup> outward diffusion. However, one can easily imagine that most real cases are found somewhere in between these two extremes. In a recent paper by Susman et al, a theoretical model for describing the general case of oxidation of spherical particles was proposed. Here, the NKE and Valensi-Carter approaches are combined. However, the Cabrera-Mott effect and grain boundary diffusion are neglected.<sup>32</sup> At the core of the model is the parameter  $\phi$  that describes how large portion of the metal volume is converted into oxide that contributes to core contraction. It is defined as

$$\phi = -Z \frac{dV_1}{dV_{ox}} \quad (2.2)$$

where  $V_1$  is the core volume,  $V_{ox}$  is the oxide volume and  $Z$  the bulk expansion coefficient of the oxide, commonly known as the Pilling-Bedworth ratio.<sup>32</sup> In the limit of  $dV_1 \rightarrow 0$ , that is, no core contraction, we find  $\phi \rightarrow 0$  corresponding to the NKE. Oppositely, when all oxidation gives rise to core contraction,  $dV_1 = -dV_{ox}/Z$  yielding  $\phi = 1$  for a pure Valensi-Carter (VC) mechanism, as depicted in Figure 2.4.

In the general case, for a spherical particle of radius  $a_0$ , the volume of the metal core  $V_1$  and the total volume  $V_2$  of metal, oxide and void, can be expressed in terms of the initial metal volume  $V_0$  as

$$V_1 = V_0(1 - \phi\delta) \quad (2.3)$$

$$V_2 = V_0(1 - \phi\delta + Z\delta) \quad (2.4)$$

where  $Z$  is the bulk expansion coefficient and the oxidized volume fraction  $\delta$  is defined as  $\delta(t) = \frac{V_{ox}(t)}{ZV_0}$ . In the limit of NKE, eq. (2.3) and (2.4) simplify to  $V_1 = V_0$  and  $V_2 = V_0(1 + Z\delta)$ .

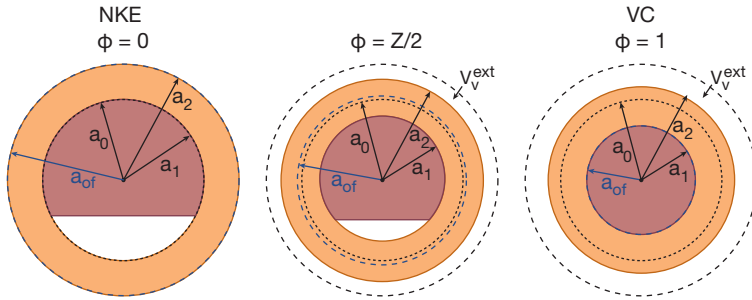


Figure 2.4: The general theoretical model. In the limit  $\phi \rightarrow 0$ , the NKE model is recovered, for which the oxidation front is at the oxide/gas interface. Correspondingly, for  $\phi = 1$ , the VC model is recovered with the oxidation front at the oxide/core interface. For  $\phi = Z/2$ , the oxide volume inside  $V_{ox}^{in}$  and outside  $V_{ox}^{out}$  the oxidation front are equally large. Adapted from Ref.<sup>32</sup>.

In the VC mechanism, the oxide/metal interface is shifting inwards due to vacancies diffusing outwards, this is known as the Kirkendall shift<sup>32</sup>. Hence, one can think of the vacancies diffusing outwards accumulating at the oxide/gas interface to an external void  $V_v^{ext}$ . I will not go into the full derivation of the expression for the Kirkendall shift from the diffusion rates. However, we can look at the case of stoichiometric inward  $O^{2-}$  and outward  $M^+$  diffusion, which means there will be no net vacancy flow and  $\phi = Z/2$ , as half of the converted oxide will give core contraction. The oxidation reaction occurs at the oxide/metal and oxide/gas interfaces. However, it can be useful to imagine an *oxidation front* as a spherical surface at radius  $a_{of}$ , which should be relative to the ratio between growth of oxide at the oxide/gas interface  $dV_{ox}^{out}$  and at the oxide/core interface  $dV_{ox}^{in}$ , respectively. For the case of  $\phi = Z/2$ , we will have  $V_{ox}^{in} = V_{ox}^{out}$ .<sup>32</sup>

This theoretical model for describing the oxidation progression was used in **paper I** in the NKE limit. In addition, assuming a straight void/core interface and a hemispherical particle, as depicted in Figure 2.5, the void volume can be expressed as

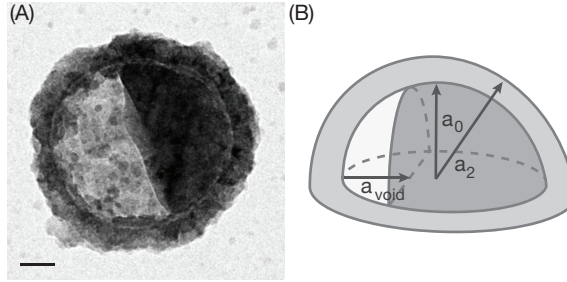


Figure 2.5: Void volume model. (A) TEM image of a Cu particle with a sharp void/core interface, according to the homogeneous NKE. (B) Hemispherical model of the void growth in the NKE limit with a sharp void/core interface  $a_{\text{void}}$  is the width of the void,  $a_0$  is the initial core radius and  $a_2$  is the radius of both core and shell.

$$V_{\text{void}} = \frac{\pi}{6} a_{\text{void}}^2 (3a_0 - a_{\text{void}}) \quad (2.5)$$

where  $a_{\text{void}}$  is the width of the void. The geometrical relation in (2.5) was used for extracting parameters for simulating the scattering response of different model geometries using the finite-difference time-domain (FDTD) method.

## 2.2.2 Suppressing void formation upon Cu oxidation

In the theoretical model described in the previous section, the effect of grain boundary diffusion is neglected. However, at the macroscopic scale it has been shown that grain boundaries can greatly increase the diffusion rates, hence also the oxidation rates.<sup>28</sup> Furthermore, it has been shown for nanowires that grain boundaries play a paramount role in void nucleation by providing vacancy sinks. At grain boundaries, there is enough energy to overcome the void nucleation energy barrier and hence vacancies can accumulate there. For Cu, the energy barrier for forming a cluster of 4 vacancies, which for Cu is the critical size for void nucleation, is 2 eV.<sup>15</sup> However, this is only true where there is a high-angle between the lattices in the two grains. In this recent paper by Huang et al<sup>15</sup>, they provided evidence that void nucleation can be suppressed at twin-boundaries in Cu nanowires. They explain the suppression of void nucleation by a Kirkendall lattice shift occurring at the metal/oxide interface, hence, it is an example of the ideal Kirkendall effect at the nanoscale (Figure 2.2).

Most papers concerning oxidation of Cu nanoparticles report on a void forming due to NKE.<sup>11–13,34</sup> However, there is one recent paper on *in situ* STEM oxidation of Cu nanoparticles where void formation is not observed.<sup>17</sup> Seemingly single crystalline nanoparticles of sizes between 6 to 80 nm are oxidized in 2 Pa O<sub>2</sub> at temperatures between 300-500°C. The oxide is nucleating at one side, and as the oxidation progresses, the sharp oxide/metal interface is moving cross the particle to the other side, showcasing an example of a Kirkendall shift since no void is forming, though it is not explicitly mentioned by the authors.

From the amount of models describing different mechanisms affecting the oxidation of metals, and in particular, metals at the nanoscale presented here, and even more so from

the amount that has not been given any space in this chapter, it is evident that this is a process of great interest. The oxidation depends on many parameters, some of which have been introduced in this chapter, such as the grain structure of the metal, the diffusion rates of metal and oxygen ions and the lattice misfit between metal and oxide. As much as it is evident that this field is of high interest, it is also evident that this chapter is nowhere near conclusive, but hopefully it can give a comprehensive enough introduction to the aspects of Cu nanoparticle oxidation presented in **paper I** and **paper II**.



# 3 NANOPLASMONICS

The terminology ‘nanomaterial’ and ‘nanoplasmonics’ that we use today to describe very tiny objects is something that developed over the past few decades. However, practical expertise about using materials on this length scale has existed for thousands of years. Already the Romans used metal nanoparticles to stain glass, as in the example of the Lycurgus cup (in Figure 3.1)<sup>37</sup> preserved until today and exhibited at the British Museum.

How can objects much smaller than the wavelength of visible light still change the color of the glass that we see? Even though these objects are far too small to be seen by naked eye, even with optical microscopes, millions of them will affect how we perceive the colored glass. The answer can be found in the electronic properties of the metal. The color of the Lycurgus cup comes from collective oscillations of the free electrons in the metal nanoparticles in the glass.

In this chapter, I will give an introduction to this phenomenon commonly referred to as *plasmonics* and we will see how this interaction between metal nanoparticles and visible light is used successfully for sensing, traditionally within biology, for detection of proteins and antibodies, but more recently in materials research and gas detection.

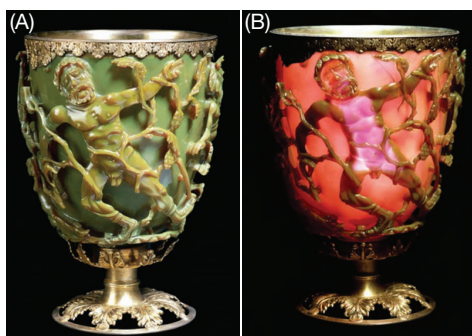


Figure 3.1: The Lycurgus cup. (A) Light is scattered from the outside and the glass appears green. (B) Illuminated from the inside, the light is transmitted through the glass and the color is crimson. Reprinted from the British Museum.<sup>38</sup>

### 3.1 Electrons in metals

To understand the plasmonic properties of metals, we need to study the interaction between their electrons and light. In physics, light is often described as a harmonic electromagnetic field  $\mathbf{E}(\mathbf{x}, t) = \mathbf{E}_0(\mathbf{x}, t)e^{-i\omega t}$ . For noble metals, the response to an applied electromagnetic field is well described by the free electron model, also known as the Drude-Lorentz-Sommerfeld model.<sup>39</sup> In this model, it is assumed that the macroscopic response of all electrons is simply the response of one electron multiplied by the electron density. Hence we start by looking at the interaction between one electron and the applied electromagnetic field. This interaction can be described by Newton's equation of motion, as it is simply a force from the applied field acting on the electron of mass  $m_e$  and charge  $e$

$$m_e \ddot{\mathbf{x}} + m_e \gamma \dot{\mathbf{x}} = -e \mathbf{E}_0 e^{-i\omega t} \quad (3.1)$$

where  $\gamma$  is the damping constant.<sup>39,40</sup> In the model, the electron is assumed to be “free”, thus the restoring spring constant is neglected in the formula. The solution to the differential equation is given by

$$\mathbf{x}(t) = \frac{e}{m_e(\omega^2 + i\gamma\omega)} \mathbf{E}(\mathbf{x}, t) . \quad (3.2)$$

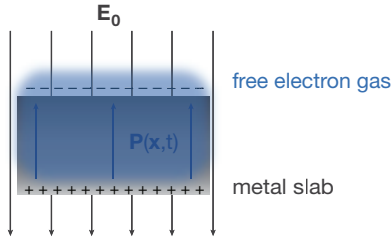


Figure 3.2: A metal slab in a static electric field. The free electrons are displaced, thereby inducing the polarization field  $\mathbf{P}$  inside the metal slab.

The macroscopic polarization field  $\mathbf{P} = -ne\mathbf{E}$  from the displacement of the electrons is depicted in Figure 3.2. The polarization  $\mathbf{P}$  acts to cancel out the applied field inside the metal. In Maxwell's equations the sum of the fields inside the metal is known as the displacement field  $\mathbf{D}(\mathbf{x}, t) = \epsilon_0 \mathbf{E} + \mathbf{P}$  where  $\epsilon_0$  is the permittivity of free space.<sup>40</sup> Rewriting it, we find

$$\mathbf{D}(\mathbf{x}, t) = \epsilon_0 \left( 1 - \frac{ne^2}{\epsilon_0 m_e (\omega^2 + i\gamma\omega)} \right) \mathbf{E}(\mathbf{x}, t) \quad (3.3)$$

and by assuming we are dealing with an isotropic and linear medium the constitutive relation  $\mathbf{D} = \epsilon_0 \epsilon \mathbf{E}$  holds, thus we have derived the dielectric function of a free electron gas as

$$\epsilon(\omega) = 1 - \frac{\omega_p^2}{\omega^2 + i\gamma\omega} \quad (3.4)$$

$$\epsilon(\omega) = \epsilon_1(\omega) + i\epsilon_2(\omega) = 1 - \frac{\omega_p^2}{\omega^2 + \gamma^2} + i \frac{\omega_p^2 \gamma^2}{\omega(\omega^2 + \gamma^2)} \quad (3.5)$$

where the plasma frequency is defined as  $\omega_p^2 = \frac{ne^2}{\epsilon_0 m_e}$ . At optical wavelengths  $\omega \gg \gamma$ , the real part of the dielectric function can be simplified to

$$\epsilon_1(\omega) = 1 - \frac{\omega_p^2}{\omega^2} \quad (3.6)$$

and the imaginary part is negligible. Resonance is achieved when  $\epsilon_1(\omega) = 0$ . Thus, the plasma frequency is the resonance frequency of the free electron gas.<sup>39</sup> As this oscillation can be regarded as harmonic, its energy is quantized and these quanta are known as plasmons, a quasi-particle.<sup>40</sup> So far, we have not made any restrictions on the geometry of the metal, thus these plasmons are volume plasmons, which, however, do not couple to photons but can only be excited by electrons. Therefore, these plasmon energies are commonly studied by electron energy loss spectroscopy (EELS). In the next section, we will narrow down the scope to surface plasmons and in particular *localized* surface plasmons.

The dielectric function in (3.4) can only accurately describe the optical response of a metal below the threshold for transitions between electronic bands, commonly known as interband transitions. However, at higher photon energies there is competition between exciting plasmon modes and electronic interband transitions, which leads to less efficient plasmon excitation and higher damping. Noble metals like Au and Ag, have completely filled d-bands from which electrons are excited to bands above the Fermi-level. For Au and Cu, this threshold is in the visible region of the spectrum, at 2.4 eV or 500 nm for Au and 2.1 eV or 590 nm for Cu. For Ag on the other hand it is at higher energy, at 3.9 eV corresponding to 320 nm in the UV region.<sup>39</sup> Due to the threshold of Au and Cu being in the visible region it leads to more damping of the plasmons compared to Ag. Fundamentally, it is interesting to consider that the threshold of the interband transitions gives the bulk metals its color. For example, Au has its yellow color because photons of shorter wavelengths, corresponding to green and blue colors, are absorbed and red and yellow are reflected. For Cu, also photons of yellow wavelengths are absorbed and only red wavelengths are reflected, whereas Ag has its threshold in the UV and all visible wavelengths are reflected.

## 3.2 The quasi-static approximation

At the beginning of this chapter, an explanation was promised to: “how is it possible that the interaction between metal nanoparticles and light can give glass different colors?”. In the previous section, we learnt that the free electrons of noble metals can oscillate collectively by excitation from an external electromagnetic field. However, so far we have not said anything about nanoparticles. In this context, nanoparticles are defined as pieces of metal much smaller than the wavelength of visible light, in at least two dimensions.

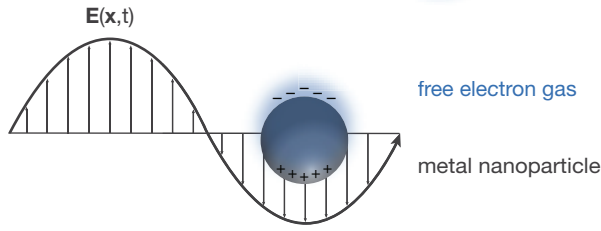


Figure 3.3: Localized surface plasmon. A schematic illustration of an external harmonic field exciting a dipolar resonant oscillation of the free electron gas in the metal nanoparticle.

Let us consider a sphere with diameter  $d \ll \lambda$ , where  $\lambda$  is the wavelength of the applied external field. In this limit, we can regard the field at any time as static over the nanoparticle but it may vary over time. In other words, it oscillates with a frequency  $\omega$ . This is called the *quasi-static* regime.<sup>39</sup> When the electromagnetic field, static over the nanoparticle,  $\mathbf{E}(t) = \mathbf{E}_0 e^{i\omega t}$  is applied, the free electron gas of the metal nanoparticle is polarized as a dipole, as depicted in Figure 3.3. The dipolar moment of the spherical particle can be written as

$$\mathbf{p} = 4\pi\epsilon_0\epsilon_m \left(\frac{d}{2}\right)^3 \frac{\epsilon - \epsilon_m}{\epsilon + 2\epsilon_m} \mathbf{E} \quad (3.7)$$

where  $\epsilon_m$  is the dielectric constant of the medium surrounding the nanoparticle. The polarizability  $\alpha$  is then defined such that we can write  $\mathbf{p} = \epsilon_m \alpha \mathbf{E}$  with

$$\alpha = 4\pi\epsilon_0 \left(\frac{d}{2}\right)^3 \frac{\epsilon - \epsilon_m}{\epsilon + 2\epsilon_m}. \quad (3.8)$$

The full derivation of the dipolar moment and the polarizability can be found elsewhere.<sup>40</sup> The resonance frequency of the dipole is found at the maximum polarizability  $\alpha$ . Now, remember that the dielectric function is dispersive  $\epsilon(\omega)$ . Thus, the resonance frequency is found by minimizing  $|\epsilon + 2\epsilon_m|$ . At optical frequencies the imaginary part of  $\epsilon(\omega)$  is small, thus it is enough to minimize the real part, which yields  $\text{Re}[\epsilon(\omega)] = -2\epsilon_m$ . This is known as the Fröhlich condition.<sup>40</sup> The resonance mode excited under this condition is called a localized surface plasmon. For a particle surrounded by air, the condition is met at the frequency  $\omega = \omega_p/\sqrt{3}$ . Hence we see that the real part needs to be negative to meet the condition for a localized surface plasmon, and in Figure 3.4 we find that the condition is met for gold around 2.5 eV, which is the approximate resonance frequency of a spherical gold nanoparticle.

An effect of the dipole resonance is an enhancement of the absorption and scattering of radiation from the metal nanoparticle. This is described by the scattering and absorption cross-sections, which can be calculated from the Poynting-vector of the enhanced field as

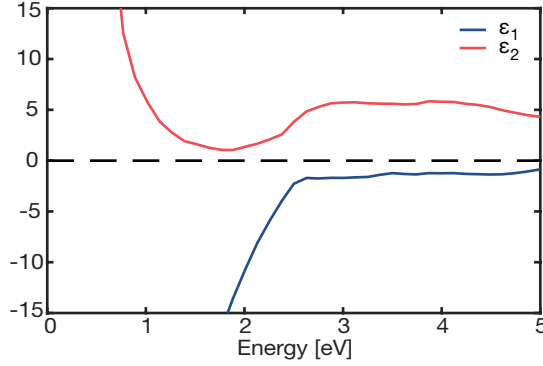


Figure 3.4: The real part  $\epsilon_1$  and the imaginary part  $\epsilon_2$  of the dielectric function of Au.

$$\sigma_{sca} = \frac{k^4}{6\pi} |\alpha|^2 = \frac{8\pi}{3} k^4 \left(\frac{d}{2}\right)^6 \left| \frac{\epsilon - \epsilon_m}{\epsilon + 2\epsilon_m} \right|^2 \quad (3.9)$$

$$\sigma_{abs} = k \text{Im}[\alpha] = 4\pi k \left(\frac{d}{2}\right)^3 \text{Im} \left[ \frac{(\epsilon - \epsilon_m)}{\epsilon + 2\epsilon_m} \right]. \quad (3.10)$$

The extinction of light interacting with the nanoparticle is the sum of the absorbed and scattered light, thus  $\sigma_{ext} = \sigma_{abs} + \sigma_{sca}$ . As the absorption cross-section scales with  $d^3$  and the scattering cross-section scales with  $d^6$ , for small particles with  $d \ll \lambda$  absorption is dominating, but as the size increases the scattering of radiation will increase faster than the absorption. Thus, for larger particles with  $d \approx 100$  nm, scattering of radiation is the dominating factor to extinction.

The same resonance condition as for the polarizability also holds for the absorption and scattering cross-sections. Thus, at the resonance frequency the scattered radiation is strongly enhanced compared to the geometrical volume of the nanoparticle. For macroscopic objects, the scattering cross-section is equal to its geometrical volume, but for nanoparticles the scattering cross-section is larger than its geometrical volume according to (3.9). Thus, the nanoparticle is perceived as much larger than its real volume. In an optical microscope, the scattering from single nanoparticles can therefore be seen. When combining millions of nanoparticles, the scattering from them is strong enough to be visible to the naked eye. In this way, the Lycurgus cup gets its color. The resonance frequency of the silver and gold nanoparticles in the glass is around 500 nm, the wavelength corresponding to green light. In Figure 3.1A one sees the green light scattered from the outside of the cup and in Figure 3.1B, when illumination comes from within the cup, the transmitted light is seen, making the glass appear red as the green light is absorbed.<sup>37</sup>

The relations for the absorption and scattering cross-sections in (3.9) and (3.10) are only valid in the limit of particles much smaller than the wavelength of the applied field. In practice, this assumption holds for spherical particles of diameter  $d < 100$  nm.<sup>40</sup> For larger particles, the quasi-static assumption is no longer valid as the electromagnetic field cannot be considered static over the nanoparticle. One can imagine that there will be a

retardation in the polarization of the free electron gas, as the electrons on one side will experience a different field strength compared to the other side. This leads to a decreased strength of the polarization field and a red-shift of the resonance energy. A second effect of a larger particle volume is increased radiation damping i.e. the collectively oscillating free electrons decays as photons, which is the strongest factor for decreasing plasmon resonance strength.<sup>40</sup> For this case, one has to apply Mie theory to correctly describe the polarizability of the particle. In Mie theory, the electromagnetic field is described as an infinite harmonic series, to be able to account for the retardation effects and radiative damping.<sup>41</sup> The resulting scattering and absorption cross-sections will also be expressed as harmonic series expansions. However, for the application in this thesis, I consider it sufficient to assume the quasi-static regime as the particles are still smaller than the wavelength of the light and possible retardation effects and radiative damping will be expressed as red-shifts of the measured scattering resonance. For the interested reader an introduction to Mie theory is given by Kreibig and Vollmer<sup>39</sup> and a more comprehensive derivation by Bohren and Huffman.<sup>41</sup>

### 3.3 Particle shape effects

In the previous section, we only considered spherical particles. With a multitude of fabrication techniques available, such as colloidal synthesis or electron beam lithography (as is discussed in chapter 4), for creating particles of more or less exotic shapes, we need to understand how the plasmon resonance is affected by the shape of the nanoparticle.

When extending the scope to more complex shapes, a natural step from the sphere is to look at ellipsoids, which as a nanoparticle is commonly referred to as a nanorod. If one excites the plasmon of a single nanorod by unpolarized light and detects the scattered radiation, one will detect not only one but two resonance modes, as depicted in Figure 3.5. Due to the high aspect ratio (AR) of the rod, the free electron gas can either oscillate along the long axis of the rod or perpendicular to it, with two different resonance energies. These two modes are called longitudinal mode (LM) and transversal mode (TM), respectively.

Upon increasing the size of the nanoparticle the resonance red-shifts, as shown for spheres, pentagons and triangles by Mock et al<sup>42</sup>. In addition, more rounded edges blue-shifts the resonance. This can be understood by referring to the previous section, i.e. that the polarization field inside a larger particle is weaker due to retardation effects, thus inducing a red-shift of the resonance.<sup>43</sup> The same argument can be used to explain the blue-shift due to rounded corners from annealing. Since the volume is the same but less extended in space, the retardation will be smaller, hence the resonance is blue-shifted.

As exemplified in Figure 3.5, finite-difference time-domain (FDTD) electrodynamic simulations<sup>44</sup>, provides a practical tool for calculating the response of different geometries and materials to electromagnetic fields. By this method, Maxwell's famous equations for describing electromagnetic fields are solved in every point of a finite mesh at different time points,<sup>45</sup> resolving how the energy from the field is dispersed in the material over time. Hence, as proved many times, it can accurately estimate the plasmon resonance energies of metal nanostructures.

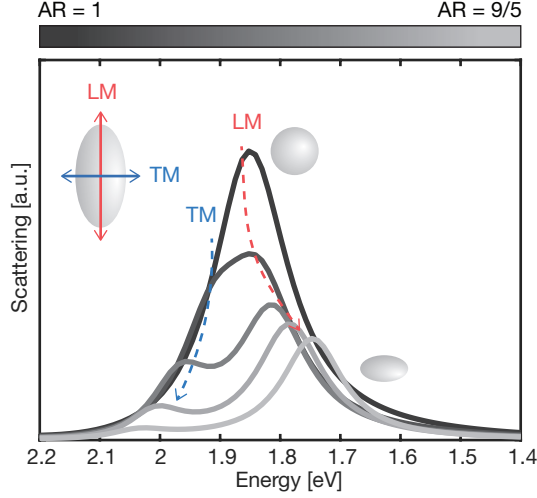


Figure 3.5: Aspect ratio dependence of the plasmonic resonance. The plasmonic resonances of a Cu sphere with  $AR = 1$  and successively increasing  $AR$  until a rod of  $AR = 9/5$  with two distinct modes, longitudinal (LM) and transversal (TM), as simulated by FDTD.

### 3.4 LSPR sensing

As has been established in previous sections, the resonance frequencies of the absorption and scattering cross-sections are dependent on the dielectric constant of the embedding medium, as well as of the dielectric function and the volume of the nanoparticle itself. These aspects are the foundation of LSPR sensing.

The early use of LSPR sensing was mainly for biological and medical purpose for detection of an analyte, e.g. an antibody in solution.<sup>7</sup> The sensor made out of gold or silver nanoparticles on a glass substrate was functionalized by receptors for the right antibody and upon binding of the analyte to the receptor, the refractive index (RI) surrounding the sensor increased and induced a red-shift of the resonance frequency, as depicted in Figure 3.6. This is refractive index based LSPR sensing and it relies on meeting the Fröhlich condition  $\text{Re}[\epsilon(\omega)] = -2\epsilon_m$ , for which the resonance frequency  $\omega_{LSPR}$  is found from the real part of the dielectric function at optical wavelengths in (3.6) as

$$\omega_{LSPR} = \frac{\omega_p}{\sqrt{1+2\epsilon_m}} . \quad (3.11)$$

If converting to wavelengths, as is often used within LSPR sensing, via the relation  $\lambda = 2\pi c/\omega$ , one obtains the following relation for the resonance wavelength

$$\lambda_{LSPR} = \lambda_p \sqrt{1 + 2\epsilon_m} . \quad (3.12)$$

The dependence of the resonance wavelength on the refractive index  $n = \sqrt{\epsilon_m}$  of the embedding medium is not linear, but over small changes of  $n$  it appears to be nearly linear.<sup>7</sup>

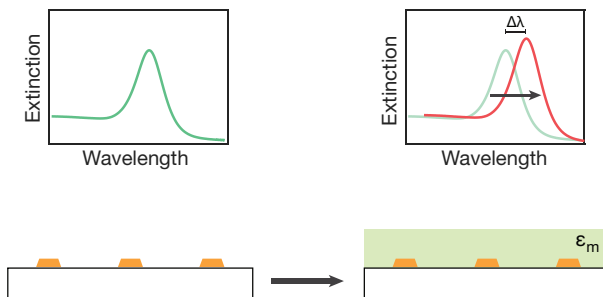


Figure 3.6: The principle of LSPR sensing. A change in the dielectric constant  $\epsilon_m$  of the embedding medium induces a shift of the LSPR, which can be measured using specific descriptors of the resonance peaks, such as peak position, width or peak extinction.

Au and Ag nanoparticles have their LSPR in the visible range of the electromagnetic spectrum, which makes them popular for sensing. Even though Ag has lower damping and thus a more narrow resonance, Au is the more common choice due to being more chemically stable.<sup>7</sup> However, other noble metals such as Cu<sup>46</sup>, Pt<sup>47</sup> and Pd<sup>47</sup> can support plasmon resonances. Even Al<sup>48</sup> has been shown to have plasmon resonances in the visible spectrum. The plasmon resonances of these more unconventional plasmonic materials have been taken advantage of for bringing LSPR sensing into the field of materials research. One example of an application of LSPR within materials research that has been studied extensively in our group is hydrogen sorption of Pd for applications within hydrogen storage and hydrogen sensing.<sup>49</sup> In this quest for more efficient hydrogen sensors, plasmonic nanoalloys have been developed and found to have interesting and unexpected properties.<sup>50–52</sup> Recently, the advantage of studying oxidation of Cu nanoparticles *in situ* by LSPR has been explored due to the technique being less invasive and simpler than *in situ* studies by environmental TEM (E<sub>0</sub>TEM).<sup>11–13</sup> Apart from material sciences, LSPR sensing has emerged within catalysis<sup>9,53</sup>.

In the mentioned methods for LSPR sensing in materials research, the resonance shift does not originate from a change in RI of the surrounding medium but rather from an intrinsic change in the properties of the nanoparticle itself, such as volume expansion or contraction, at the same time as the material itself is changed as in the case of Pd hydrogenation<sup>49</sup> or Cu oxidation<sup>13</sup>. Generally, there are two approaches to LSPR-based materials research. In the first case, a plasmonic antenna is positioned next to the nanomaterial subject to the investigation, which is advantageous if the nanomaterial is not plasmonic, too small<sup>54</sup> or loses its plasmonic properties as in the case of Cu oxidation<sup>11</sup>. In the second case, the scrutinized nanomaterial itself is the sensor.<sup>13,55</sup> Since the nanoparticle size and shape along with its dielectric function has been mentioned as factors influencing the resonance frequency, a change to any of those will induce a detectable resonance shift.

## 3.5 Single nanoparticle plasmonics

For understanding the exact dependence of the plasmon resonance on particle specific properties, such as shape and size, as discussed in section 3.3, one needs to study the particles one by one. As soon as an ensemble of many particles is studied, the response will be an average over the whole ensemble and small differences in shape or size cannot be scrutinized.

A common method for studying plasmon resonances of single nanoparticles is dark-field scattering spectroscopy (DFSS), which I will discuss in more detail in chapter 5. DFSS is called a far-field technique, as it probes the scattered radiation far from the source. Other examples of far-field techniques are photothermal imaging where heating due to absorption is studied<sup>56</sup> or surface enhanced Raman spectroscopy (SERS), where the field enhancement is exploited in order to increase the Raman scattering<sup>57</sup>. Apart from far-field techniques, there are also techniques that can probe the plasmon resonance very close to the particle, by for example a tiny tip (scanning near-field optical microscopy<sup>58</sup>) or an electron beam (EELS<sup>59</sup> or cathodoluminescence<sup>60</sup>). As DFSS is the technique used for probing the plasmon resonances in this thesis, for the rest of this section I will focus on this technique.

DFSS and other far-field field techniques are intrinsically diffraction limited, as explained by Abbé's law<sup>58</sup>  $\Delta x = \lambda / (2\pi NA)$ , where  $NA$  is the numerical aperture of the objective. In practice, this means that objects that are not further apart than  $\Delta x$  cannot be distinguished but appear as one object. Hence, this needs to be considered when designing samples for single particle scattering experiments. The  $NA$  depends on the magnification of the objective. To illustrate this, let's take the example of the dark-field objective I used for the DFSS measurements with  $NA = 0.6$ . At a wavelength of  $\lambda = 700$  nm, this gives  $\Delta x \approx 200$  nm, which means that objects less than 200 nm apart cannot be resolved as individual point sources.

Another aspect to be aware of, is the array effect from coupling between plasmonic nanoparticles. At shorter interparticle distances, the near-field interaction is stronger and can induce a shift of the resonance. This effect decays as  $d^{-3}$ , thus at distances a few times larger than the particles it is negligible. At larger particles distances, particles couple by the far-field through diffraction. This effect is more long-range and decays as  $d^{-1}$ . It can either increase or decrease the linewidth and blue-shift or red-shift the resonance, depending on the interparticle distance.<sup>40</sup>



# 4 NANOFABRICATION

Today, nanotechnology exists in our everyday life. Through discoveries in the field, the size of our computers has decreased at the same time as the computer power has increased by more than a million times.<sup>61</sup> This has been possible due to the tremendous development of nanofabrication techniques, some of which I will touch upon in this chapter.

Richard Feynman asked in 1959, in his famous talk *There is plenty of room at the bottom*, why it was not already possible to write “the entire 24 Encyclopaedia of Britannica on the top of a pin”.<sup>62</sup> A few decades earlier, the transmission electron microscope had been invented,<sup>63</sup> which had enabled seeing objects smaller than a bacteria. However, so far, these objects could only be studied but not manipulated or let alone fabricated by humans. It was not until the early 1980’s when the first steps in modern nanofabrication were taken, through the development of scanning tunnelling microscopy that enabled seeing and manipulating single atoms.

Over the past 40 years, the nanofabrication techniques have been refined over and over again in the quest to reach ever-higher control and resolution in terms of feature size. Fundamentally, one can divide all nanofabrication techniques into two different approaches, that is, either growing structures on a flat substrate, which is known as *bottom-up* fabrication, or sculpturing structures out of a surface, the *top-down* approach. The samples studied in this thesis have been fabricated by the bottom-up approach, thus emphasis will be put on explaining this branch of nanofabrication.

## 4.1 Lithography

In both bottom-up and top-down nanofabrication, a commonly used approach is lithography, which in general terms means to produce a patterned mask through which the material of choice can be deposited. Common steps for almost all lithographical methods are, firstly, spin-coating of a polymeric mask, secondly, patterning of the mask for example by exposing some parts of the mask to electrons or photons, or by employing self-assembly of colloidal beads to produce the pattern. Thirdly, holes are etched through the mask either by wet or dry etching. When the mask is produced, the material of choice can be deposited through the mask to reproduce the pattern on the

substrate. There is one final step, the removal of the mask from the substrate, this is commonly known as lift-off.

A multitude of different methods for patterning the mask have been reported and these are three of the most common methods; to use photons as in photolithography, electrons as in electron-beam lithography (EBL) or self-assembly of colloidal beads as in colloidal lithography. The two former methods provide more precise control of the pattern, whereas in the latter method one has to trust the interaction between the nanosized colloidal beads to produce the pattern. On the other hand, colloidal lithography provides a simple way of covering large areas with arrays of nanoparticles. Common for all three techniques is to use a polymeric mask, however in photolithography or electron-beam lithography it needs to be sensitive to photons or electrons, respectively. After exposure of the mask to the beam, a wet chemical ‘developer’ is used that reacts with and removes the exposed areas of the mask to create the holes, whereas in the case of colloidal lithography the colloidal beads determine the pattern of the mask and the exposed areas are removed by oxygen plasma etc.

Two lithographical techniques have been employed for preparing the samples I used in the work of this thesis, namely electron-beam lithography and colloidal lithography. Therefore, I will give a more thorough introduction to these methods below, followed by a detailed description of each step of the methods.

#### **4.1.1 Colloidal lithography**

Colloidal lithography is based on self-assembly of colloidal beads on a sacrificial mask layer, producing either a close-packed array or a less dense quasi-random array. By colloidal lithography large areas can be covered with nanoarrays in a cheap and simple way. Adding some creativity, complex shapes of particles can be fabricated, such as triangles, cones or hollow nanovolcanos<sup>64</sup>. Nanotriangles, for example, can be made from the traditional colloidal lithography when a close-packed array of colloidal spheres is used as a mask. Whereas by the method used in this thesis, hole-mask colloidal lithography (HCL) developed by Hans Fredriksson et al<sup>65</sup>, one can make nanodisks or cones arranged in a quasi-random array.

#### **4.1.2 Hole-mask colloidal lithography**

Compared to traditional colloidal lithography, that is the mask is made of a close-packed array of colloidal spheres rather than a patterned polymer layer, HCL combines the use of a polymeric mask - as in electron beam lithography - with colloidal spheres for patterning of the mask (Figure 4.1). A spin-coated polymeric mask (typically poly(methyl methacrylate) (PMMA)) is patterned by drop-casting a positively charged polyelectrolyte layer (typically poly(diallyl dimethylammonium) (PDDA)) and sequentially the negatively charged polystyrene (PS) beads. They will distribute randomly over the surface with a density defined by the electrostatic repulsion between the negatively charged surfaces of the PS beads. The hole-mask itself is a thin metallic film physically evaporated on top of the colloidal spheres, in which holes are formed by the shadowing-effect of the PS beads during the metal evaporation. These holes are subsequently exposed by removing the colloidal beads by means of tape-stripping and transferred into the polymer layer by

oxygen plasma etching down to the substrate. Now, the substrate is exposed at the position of the patterned holes in the mask, thus thin film evaporation of a metal of choice will result in tapered nanodisks growing on the substrate. The tapering of the resulting nanodisks originates from the narrowing of the hole during deposition. Hence, if evaporation is continued long enough, the disks will turn into cones. This effect can be further explored to craft more complex nanostructures, as demonstrated by Svetlana Alekseeva (former Syrenova) et al<sup>66</sup>, in our group. Finally, the polymeric mask needs to be removed to render solely the final pattern on the substrate. This is easily done by dissolving the mask in acetone, which is commonly known as lift-off.

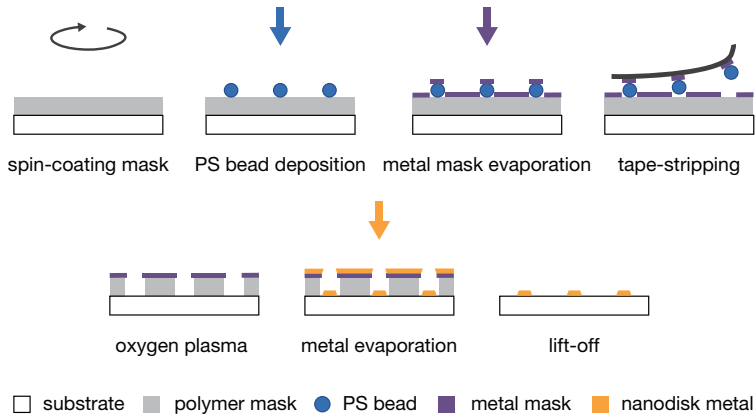


Figure 4.1: Hole-mask colloidal lithography. In short, the HCL protocol involves the steps depicted here; polymer mask spin-coating, PS bead electrostatic self-assembly, metal mask evaporation, tape-stripping and sequential oxygen plasma etching, metal disk deposition and finally, mask lift-off.

### 4.1.3 Electron-beam lithography

This technique is, as the name reveals, based on electron beam patterning of the spin-coated polymer, also known as the ‘resist’. In beam-based lithography, as photolithography also belongs to, the spatial resolution is limited by the wavelength of the accelerated particles. Electron-beam lithography will give higher resolution compared to photolithography, down to a few nanometer in resolution, since electrons can be accelerated to higher energies, thus shorter wavelengths than the optical energies of photons traditionally used. However, by UV-light, sub-100 nm resolution photolithography has been achieved<sup>67</sup>. In electron-beam lithography, opposed to photolithography where the whole surface is exposed at once through a pre-defined mask, a focused electron beam is raster-scanned over the resist to expose *a priori* defined areas of the resist to the electron beam. During exposure the resist is chemically changed, Depending in the polymer, either the solubility of the resist is increased, which results in the exposed areas being removed by the developer. This type is called a positive resist. Alternatively, exposure induces cross-linking in the resist making it less soluble, resulting in the unexposed areas being removed. This type is known as a negative resist.

The advantage of electron-beam lithography compared to self-assembly techniques, such as colloidal lithography, and the reason why it was used in this thesis, is the high control of the pattern. It is written by the pre-programmed raster-scanning beam, enabling high control and the possibility of making complex patterns. However, electron beam lithography is not suitable for covering large surfaces, since the writing time is on the order of 24 hours to cover 1 cm<sup>2</sup>.<sup>68</sup> For this reason one would rather use a method of less pattern control, such as hole-mask colloidal lithography, to cover large surfaces.

## 4.2 Spin-coating

The first step of most lithographical techniques is to produce the polymeric mask, which is typically done using a spin-coater. A spin-coater can cover samples of a few mm<sup>2</sup> up to wafers of several inches in diameter with a flat polymeric film of precise thickness. The thickness of the film is controlled by the spin rate and spin time, which is specific for each polymer. Typically spin rates are a few thousand rpm and spin times are on the order of one to a few minutes. During spinning, the sample is attached to the spinning chuck by vacuum. Thus, when spin-coating on a substrate of a few tens nanometer thin SiN<sub>x</sub> membrane supported on Si used for TEM imaging, one needs to protect the membrane for it not to break from the high pressure gradient due to the vacuum on the backside. To protect the SiN<sub>x</sub> membrane, a rigid tape attached to the silicon support from the backside, thus not in contact with the membrane, enables spin-coating and removal after spinning.

Typically, the polymer film is soft-baked after spin-coating. In electron beam lithography this step is also known as prebaking. During baking, the solvent is evaporated, yielding a solid polymer film. In some polymers the baking is also inducing cross-linking, thereby increasing the strength and durability of the film.

## 4.3 Etching

Etching methods can fundamentally be divided into two groups, dry and wet etching. Wet etching involves, as the name implies, etching by a liquid chemical, whereas dry etching removes solid material either physically or chemically (or both) by reactive ions in gas phase or plasma. The appropriate etching method can be chosen by considering the advantages of each technique. Chemical dry etching by plasma excited with a high energy radiofrequency field has high selectivity. For example can oxygen plasma be used to clean substrates from organic dirt or to remove polymer resist. This type of plasma etching is isotropic, which means material is etched not only downwards but also sideways under the mask. In HCL, this is commonly known as the under-cut (Figure 4.1) since the polymer under the metallic mask is etched but not the metal. The amount of under-cut can be tuned by varying the time of the oxygen plasma step. Apart from chemical dry etching, there is also physical dry etching - typically a beam of ions mills off material from the surface upon impact. This method has low selectivity and low speed. There are also combined physical-chemical dry etching methods, such as reactive ion etching, when ions are accelerated towards the surface to achieve higher etch rates

and give less isotropic etch. These are of importance in top-down fabrication when material is removed by etching to create the final structures.

Chemical wet etching has, similarly to chemical dry etching, high selectivity. This means it can be used to etch down material through a mask. Most wet etchants give an isotropic etch result, except for KOH etching of Si, which has high selectivity for crystal orientation.<sup>69</sup>

## 4.4 Thin film deposition

After creating the mask, the material of choice is to be deposited as a thin film to yield the final nanostructures. There exist several techniques to choose from to achieve thin film deposition. Thus, which method to choose, depends on the material and the thickness of the film to be deposited. Dielectric materials are often deposited by chemical vapor deposition, where gaseous reactants react with the heated substrate to form a solid film. By introducing the gaseous reaction agents one at a time and letting them react with the surface, atomically thin layers are achieved. This approach is commonly referred to as atomic layer deposition.

Metallic thin films can be deposited by physical vapor deposition, either by evaporation or sputtering. All evaporation techniques require heating of the source, e.g. by an electron beam hitting the source (Figure 4.2A) or resistive heating (Figure 4.2B). Above a critical temperature, the source material evaporates either directly from the solid state, which is known as sublimation, or from the liquid state. Evaporation is directional, which is advantageous for deposition through a mask, since covering the walls of the polymer mask hinders the final lift-off step. The deposition is done in a vacuum chamber to reduce collisions with gas molecules in the trajectory of the vaporized atoms and to reduce gaseous contaminations in the resulting thin film. The Cu nanoparticles that I have studied in this work were grown by electron beam evaporation.

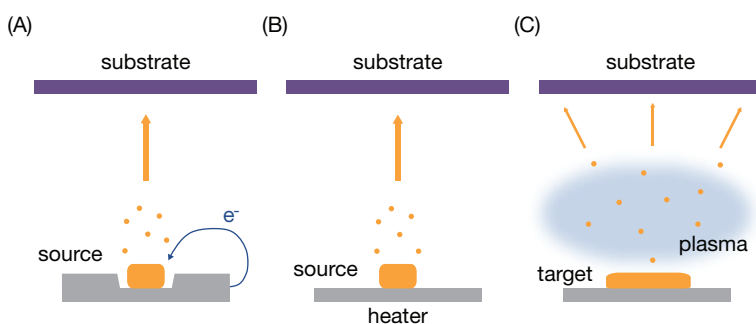


Figure 4.2: Physical vapor deposition. Three methods for physically depositing thin films, (A) electron beam evaporation employed for depositing the Cu nanoparticles, (B) thermally heated evaporation and (C) sputtering.

The second commonly used technique for metallic thin film deposition is sputtering (Figure 4.2 C). Here, an inert gas, often Ar, is ionized to a plasma by for example an

electromagnetic radiofrequency field and bombarded onto a target material, thereby ejecting atoms from the surface of the target in all directions. Hence, sputtering is not directional. The advantage of sputtering compared to evaporation is that the deposition rate is faster and alloys can with convenience be deposited using a target comprised of two or more materials.<sup>69</sup>

# 5 MICROSCOPY

Optical microscopes have been used for several centuries to study biological specimens. However, as fabrication techniques are developed for miniaturizing electronics and sensors etc., the need for imaging even smaller objects than bacteria or cells has emerged. To this end, a multitude of optical microscopes that can go beyond Abbe's diffraction limit have been developed over the past decades. Furthermore, the electron microscope was invented almost one hundred years ago<sup>63</sup> and has since been further developed to achieve resolution below  $1 \text{ \AA}$ <sup>70</sup>, enabling imaging of single atomic columns.

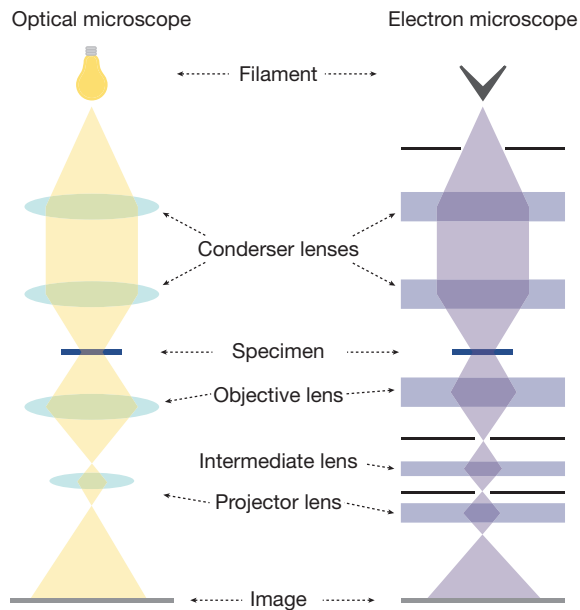


*Figure 5.1: Schematic illustration of the principles of optical and electron microscopy. The basic principles of optical and electron microscopy are fairly similar, as visualized in this drawing.*

The principle of optical microscopy and electron microscopy (Figure 5.1) is in many aspects similar. The largest difference is perhaps a fundamental one: electrons can carry

much higher energies than optical photons, thereby enabling higher resolution since the diffraction limit depends linearly on the wavelength. In both microscopes, a filament is heated to eject particles, either photons or electrons. The particles are then manipulated through a series of condenser lenses (the number can vary between setups), whose purpose is to collimate the beam and focus it onto the specimen. Here, I have depicted the beam being transmitted through the specimen in both cases, which is true in many optical microscopes, but not in all cases, as we will see in the next section. In transmission electron microscopes (TEM), the electrons are transmitted through the specimen as depicted above. Moreover, another common microscopy technique is scanning electron microscopy (SEM), where the electrons scattered from a bulk specimen are collected, hence no transmission occurs. This method will be introduced further down. Anyhow, after the specimen, the beam is passing through the objective and projector lenses, which are magnifying the image and projecting the virtual image seen either in the eyepiece of an optical microscope or on the fluorescent screen of a TEM. For digital analysis, the beam can be collected on a CCD chip.

The techniques used in the work of this thesis are TEM, SEM and dark-field scattering spectroscopy (DFSS), which is a type of optical microscopy specialized for visualizing and collecting the light scattered from single nanoparticles. These techniques will be further introduced in this chapter, along with atomic force microscopy (AFM), which was used for characterizing the Cu nanoparticles.

## 5.1 Dark-field scattering spectroscopy

In chapter 3, the formula describing the scattering cross-section of a spherical nanoparticle much smaller than the wavelength of light was presented. We saw that it depends on the diameter  $d$  as  $d^6$ . Hence, at the plasmon resonance frequency, the scattering appears to stem from a volume larger than the geometrical volume of the nanoparticle. Therefore, due to the strong scattering at the resonance frequency, metallic nanoparticles are visible in an optical microscope as individual point sources beyond the diffraction limit. In practice, Au disks with diameter  $d > 60$  nm scatter strongly enough to be detectable. Since the plasmonic resonance of Cu is not as strong as for Au, the corresponding limit for Cu is approximately  $d > 80$  nm for a disk-like particle with a height of 20-30 nm. For a spherical particle, the volume for the same diameter is larger, hence the critical diameter will be smaller.

Another important ingredient for detecting single nanoparticles, apart from the scattering cross-section, is the use of a dark-field objective. 'Dark-field' is referring to that the light emitted from the light source that has not interacted with the specimen is not collected by the objective and thus not a part of the image seen in the eyepiece or collected on the CCD chip. Practically, this is realized by illuminating at a high angle. In this way, only light back-scattered from the specimen is collected by the objective, as depicted in Figure 5.2, and a dark background is achieved from which single nanoparticles can be distinguished. An example of an image collected by a dark-field objective is seen in Figure 5.3A.

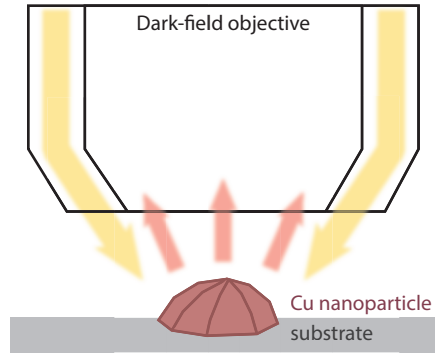


Figure 5.2: Schematic illustration of a dark-field objective used for collecting scattered light from single nanoparticles. The incoming light hits the sample at a high angle compared to the normal of the surface. Hence, only light scattered backwards is collected by the objective.

So far, I have mentioned two out of three words from the heading of the chapter: dark-field and scattering. In other words, only the spectroscopy part remains (I also note that it is possible to do analysis of single nanoparticles by solely studying the intensity change in the scattered light<sup>71</sup>, as a resonance frequency shift is often accompanied by a change in scattered intensity). Spectroscopy is required to study features in the scattering spectrum as a function of wavelength, such as to detect a shift in resonance frequency or a change in peak width, since both these parameters are descriptors used for plasmonic sensing. To enable spectral analysis, the scattered light collected by the objective is coupled into a spectrophotometer with a grating that splits the collected light into its spectral components, yielding a spectrum of the intensity at each wavelength (Figure 5.3B).

Since any real light source has a non-uniform distribution of intensity at different wavelengths, the lamp spectrum needs to be deconvoluted from the detected light scattered from the nanoparticles  $I_{signal}$ . To achieve this, the spectrum of the light source,  $I_{lamp}$ , is collected by illuminating a white object that scatters light at all wavelengths with roughly even efficiency, such as a diffuse reflectance standard. Furthermore, to isolate the light scattered solely by the nanoparticle, the light scattered by the substrate,  $I_{background}$ , has also to be subtracted. Hence, to obtain the spectrum of the scattered light from a single nanoparticle,  $I_{particle}$ , the following relation was used

$$I_{particle} = \frac{I_{signal} - I_{background}}{I_{lamp}}. \quad (5.1)$$

$I_{background}$  is collected from both above,  $I_{background}^{above}$ , and below,  $I_{background}^{below}$ , the nanoparticle scattering on the CCD chip, as visualized in Figure 5.3B. Hence, the total background signal is obtained by adding  $I_{background} = I_{background}^{above} + I_{background}^{below}$ , resulting in that the background  $I_{background}$  is collected from the same number of pixels as  $I_{signal}$ . Furthermore, by collecting the background intensity continuously for every data point of the scattering from the nanoparticle, fluctuations in the background

scattering can be accounted for and thus be eliminated from the data. The scattering spectrum from a single Cu nanoparticle calculated using eq. (5.1) is visualized in Figure 5.3C. Note that the wavelength is converted into photon energy by the relation  $E = hc/\lambda$ , where  $h$  is Planck's constant and  $c$  the speed of light.

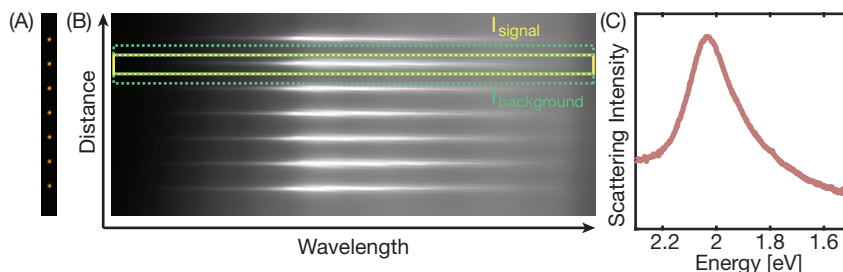


Figure 5.3: The working principle of DFSS. (A) A photograph of the light scattered from 7 Cu nanoparticles of 100 nm diameter and 40 nm thickness, collected through the dark-field objective. (B) Using a grating, the light is dispersed into its spectral components, which then are collected by a CCD chip, thereby providing an image where the intensity corresponds to the scattered intensity at each wavelength. The yellow box indicates the area from which the scattering intensity  $I_{\text{signal}}$  was integrated. The green, dashed boxes depict the areas from which the background scattering  $I_{\text{background}} = I_{\text{background}}^{\text{above}} + I_{\text{background}}^{\text{below}}$  was integrated. (C) A scattering spectrum collected from a single Cu nanoparticle, calculated by eq. (5.1).

## 5.2 Transmission electron microscopy

The basic principle of TEM depicted above in Figure 5.1 is in many ways similar to that of optical microscopy. Instead of optical lenses made for focusing photons, magnetic lenses that bend the path of the electrons by a strong magnetic field, are used.<sup>72</sup> As the beam hits the specimen, the electrons that are transmitted through the material without scattering or scattering by a low enough angle that they can pass through the aperture, can either be seen on a fluorescent screen or are collected on a CCD chip to then convert them into a digital image. Hence, the contrast of the image is determined by how many electrons that are scattered. A thicker area of the specimen will scatter more electrons, thus it will appear darker in the image. Similarly, atoms with higher atomic mass scatter more electrons, making them appear dark in the resulting image. This type of imaging is known as bright-field, since areas where few electrons are scattered appear bright in the image.<sup>72</sup>

A typical sample for studying nanoparticles commonly consists of a thin substrate, often made of  $\text{SiN}_x$  and referred to as *membrane* since it is very thin, around 20-30 nm. The nanoparticles of interest are placed on top of this membrane, either by dissolving in ethanol and drop-casting or by means of nanofabrication. For imaging Cu nanoparticles in the work of this thesis, TEM  $\text{SiN}_x$  membranes of thickness 25 nm supported on Si were produced in-house to enable further nanofabrication of the Cu nanoparticles on top.<sup>73</sup> Due to the thickness of the particles, high-resolution imaging is difficult. To this end, a Cu nanoparticle with 100 nm diameter and 40 nm thickness, imaged by a Fei Titan

80-300 at acceleration voltage 300kV, is presented in Figure 5.4. Above the grain boundary, imaged at high magnification in Figure 5.4.B, the lattice fringes from diffraction in the lattice planes are visible. However, the crystal orientation of the grain underneath the boundary is such that the fringes are not visible.

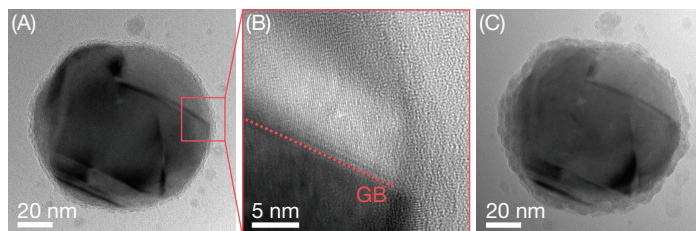


Figure 5.4: A Cu nanoparticle imaged by TEM. (A) A thin oxide layer is visible around the metallic Cu core. (B) A grain boundary imaged at high magnification. Above the grain boundary the fringes from the lattice planes are showing in one direction. (C) After high-resolution imaging for some minutes, the polycrystalline oxide shell has grown in thickness.

In crystalline or polycrystalline samples, one can obtain information about the crystal lattice by studying the diffraction from the atomic planes in the crystals which follow the Bragg condition for diffraction.<sup>74</sup> Interference will occur at a distance from the primary beam relative to the lattice plane spacing. For a single crystal, the interference will be in single spots and for polycrystals, rings will appear at the same distance from the primary beam, since several crystals with different orientation give rise to the interference. To study the Bragg diffraction, a small probe is need and achieved either by focusing the beam to a small spot or by inserting the selected-area aperture in front of the intermediate lens.

Any lens, optical or magnetic, has some imperfection resulting in that rays refracted at the edge of the lens are more strongly focused compared to rays refracted at the center of the lens. Hence, even if the beam is parallel when arriving at the lens, it will not be focused in one spot on the other side of the lens. This is known as *spherical aberration*.<sup>72</sup> To achieve high resolution, aberration correction algorithms are implemented to correct for the inherent defects of the lenses. There is also a second type of aberration, namely *chromatic aberration*, that is, the focal length of the magnetic lenses depends on the kinetic energy of the electrons.<sup>72</sup> Hence, a more monochromatic beam will lead to less chromatic aberration. Therefore monochromators are required to achieve high resolution TEM imaging.

In the field of catalysis, *in situ* TEM, also known as environmental TEM, studies are of significant interest since they enable the observation of changes to the catalyst nanoparticles during the reaction, such as structural changes<sup>75</sup>, atomic diffusion or oxidation state changes<sup>16</sup>. However, there are practical issues related to increasing the pressure in the column, since high vacuum is required to minimize electron scattering from gas molecules. A gas pressure of a few mbar can be acceptable in a volume around the sample, separated by apertures from the rest of the column to minimize diffusion of gas molecules. Specialized TEM membranes with evaporated heating spirals on the

membrane enable fast localized heating, with low thermal drift. Recently, environmental cells, where gas or liquid is encapsulated between two membranes have emerged. In such solutions, the volume enclosed by the two membranes is very small and therefore up to atmospheric pressure can be reached without compromising the quality of the imaging too much.<sup>72</sup> Hence, *operando* catalyst conditions can be reached.<sup>18</sup> However, the kinetics of catalytic reactions are governed by energy barriers, thus adding energy to the system by high energy electrons used for the imaging may change the kinetic barriers of the system, e.g. oxidized Cu nanoparticles have been shown to reduce under the beam.<sup>19</sup> During TEM imaging of Cu nanoparticles, I have observed both reduction of oxide crystals from beam exposure, as well as increased oxide growth. The latter is depicted in Figure 5.4C, where, after some minutes of high magnification imaging, the oxide shell has grown in thickness, as evident by comparing to Figure 5.4A.

### 5.3 Scanning electron microscopy

TEM is useful to study the crystal lattice and to achieve atomic resolution. However, for the study of bulk specimens that only require resolution down to a few nm<sup>72</sup>, scanning electron microscopy (SEM) is preferable. SEM is easier to operate and it is cheaper. Since the acceleration voltage is lower (usually up to 30kV), smaller and fewer lenses are required compared to TEM,<sup>72</sup> where the acceleration voltage usually is a few hundred kV. Instead of creating an image by illuminating the whole area at once as in TEM, a focused electron beam is raster-scanned over the surface and the scattered electrons are detected to create a digital image. Two types of scattering are commonly detected, either *backscattering* of the electrons from the probe or electrons ejected from atoms just below the surface, known as *secondary electrons*.

Backscattered electrons have interacted elastically with the atom cores of the material. The volume that the electrons can penetrate into is known as the interaction volume, and it depends on the beam voltage and the atomic number. For heavier atoms there is a higher probability of interaction with the atomic cores. Hence the beam voltage has to be increased to achieve deeper penetration.<sup>72</sup> Secondary electrons are ejected from atoms in the interaction volume when primary electrons from the beam interact inelastically with atomic electrons. The secondary electrons do not have as high kinetic energy and can only escape from a few nanometers depth. Hence, detecting the secondary electrons yields an image of the surface topology.<sup>72</sup>

### 5.4 Atomic force microscopy

Apart from optical and electron microscopy, atomic force microscopy (AFM) has been used in the thesis work to measure the height of the Cu nanoparticles. The principle of AFM is closely related to that of scanning tunneling microscopy (STM). In both cases, a tip raster-scans the surface. In STM, the tunneling current from the surface to the tip is measured. In AFM, however, the surface does not need to be conductive, since instead of the tunneling current the forces from the surface atoms acting on the tip are detected. AFM can be operated in two different modes. In the first one, the cantilever, on which the tip is attached, is held static when scanning the sample and cantilever deflection

creates the image. The second mode of operation is dynamic or tapping-mode AFM, in which the cantilever is vibrating and changes of the vibration amplitude or frequency are recorded. In the tapping mode, the tip is usually far enough from the surface to be attracted to it by van der Waals forces. The height profile of a Cu nanoparticle annealed at 400°C in 4% H<sub>2</sub> for 24 hours (evaporation thickness 40 nm), as obtained by tapping-mode AFM, is shown in Figure 5.5.

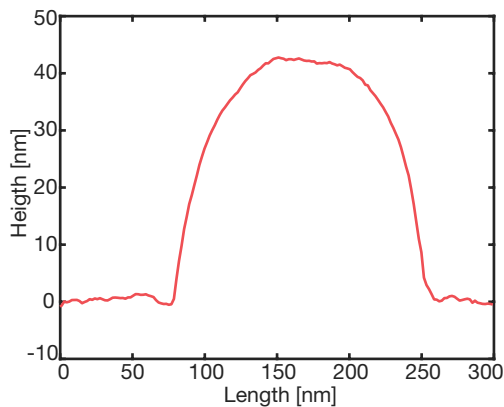


*Figure 5.5: AFM profile of a Cu nanoparticle annealed at 400°C, for 24 hours in 4% H<sub>2</sub> in Ar carrier gas.*



# 6 A CORRELATIVE DFSS AND TEM METHOD

In the previous chapter, the general principles of microscopy, in particular dark-field scattering spectroscopy (DFSS) and transmission electron microscopy (TEM), were introduced. In this chapter, I will present the four main steps of my correlative method based on those two techniques, DFSS and TEM. The main steps of the correlative method are the following: (i) initial annealing, (ii) pre-oxidation TEM imaging, (iii) DFSS *in situ* oxidation measurement and (iv) post-oxidation TEM imaging. I will reveal the small, but important and many times crucial, tips and tricks that I have learnt to be necessary for achieving a successful correlative DFSS and TEM measurement sequence.

## 6.1 Initial annealing

As the first step, after fabrication of the Cu nanoparticles, I always anneal the sample in reducing environment. This is necessary for various reasons. (i) First of all to achieve a controlled grain structure of the reduced nanoparticles, since the evaporation of Cu for growing the particles yields a highly polycrystalline and undefined grain structure. (ii) Secondly, the samples have been stored in air after fabrication. Hence, the annealing step provides a common reference point, and samples that are at least up to a few months old seem to acquire a grain structure distribution equivalent to fresh ones after the annealing step. (iii) Heating of the sample prior to TEM imaging reduces the carbon polymer deposition caused by the beam.<sup>76</sup> The carbon coating will change the oxidation kinetics, as carbon coated Cu nanoparticles have been shown to be effectively protected from oxidation.<sup>77</sup>

By tuning the annealing parameters, such as annealing temperature and time, I have achieved different grain structure distributions, as presented in Figure 6.1. The annealing conditions used in **paper I** and **paper II** are 300°C or 400°C for either 12 or 24h. However, it seems rather like the temperature than the duration, after some critical initial time, is determining the end grain structure, as apparent when observing the grain number distributions in Figure 6.1. Since the annealing has to be in a reducing environment, I used a mixture of 4% H<sub>2</sub> and 96% Ar. To this end, it is crucial that no air is leaking into the reactor, as O<sub>2</sub> partial pressure of a few mbar<sup>17</sup> is enough to oxidize Cu nanoparticles at these high temperatures even in the presence of a reducing agent.

For this reason, as well as the optical access of the microscope, to enable monitoring of the scattering resonance during the annealing, I performed the annealing in the same reactor cell (Linkam THMS600) as the subsequent *in situ* oxidation measurements.

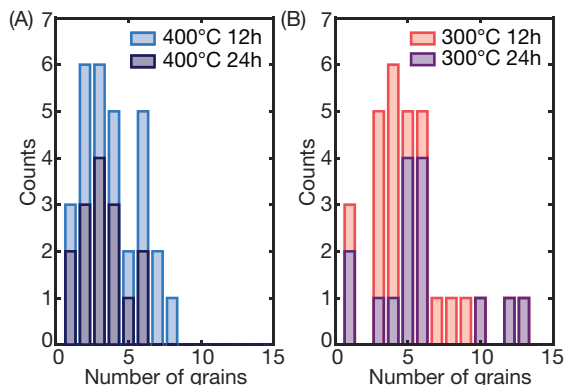


Figure 6.1: Comparison of grain number distribution depending on annealing conditions. Four samples of 15 particles each annealed at 400°C for 12 or 24 hours, respectively (A) or annealed at 300°C for 12 or 24 hours (B). The lower annealing temperature results in a larger variation in grain number as well as in a larger number of particles with up to 10 grains or more.

## 6.2 Pre-oxidation TEM imaging

After the initial annealing step, described in the previous section, I take the sample immediately from the reactor cell, where it has been kept either in the 4% H<sub>2</sub>/96% Ar mixture or in pure Ar to prevent pre-oxidation and contamination by hydrocarbons, to insert it into the TEM. For the correlative-measurement TEM imaging, as described here, I used a FEI Tecnai T20 (LaB6 filament, operated at 200kV). However, for the high-resolution imaging, a FEI Titan 30-800 was used. Even though the initial annealing step reduces the amount of carbon contamination on the particles, I experienced that the particles had slower oxidation kinetics if they had been imaged longer, say several minutes instead of less than 30 s per particle, which was the usual time for the correlative-measurement imaging. This is the reason, why the TEM imaging in the correlative-measurement-sequence was done at a lower resolution, since acquiring high-resolution images requires longer focusing times for each particle. The second reason is that long imaging can also induce oxide shell growth. I anticipate that this was more dominant when the sample was not taken directly from reducing or inert environment after annealing, but had been kept in air for some hours or days. The reason might be that under such conditions it is possible that oxygen can be stored in the substrate, which later is released under the vacuum conditions in the TEM column.

During my work, I have also developed the habit of collecting a single scattering spectrum of the particles after every step in the correlative-measurement-sequence, since the LSRP peak position can be used as an indicator for changes in or around the nanoparticle. For example, a small red-shift of the resonance peak after the TEM compared to before could be observed, however, following the precautions described

here it was very small and did not seem to affect the following oxidation kinetics significantly. An example of the scattering spectrum of a Cu nanoparticle collected before and after the pre-oxidation TEM imaging is presented in Figure 6.2. The observed red-shift probably was due to a thin oxide shell growing during imaging, however, often no oxide shell could be resolved, indicating that it, if there, was very thin. There is at least one report on a TEM-induced red-shift, observed in a LSPR-TEM correlative study<sup>78</sup>, where the authors suggest that the reason for the observed red-shift is oxidation of the Au-Ag hollow particles during TEM imaging.

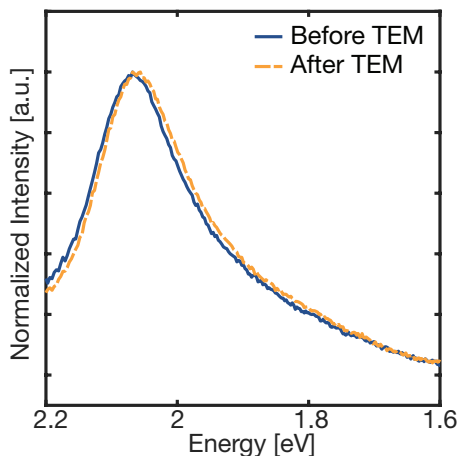


Figure 6.2: The scattering resonance before and after the pre-oxidation TEM imaging, a slight red-shift of the resonance energy is observed.

After the initial TEM imaging, the grain structure baseline of each particle was established. Based on the TEM images, I defined 5 grain structure groups which were used to investigate how the kinetics of the oxidation depend on the grain structure, in **paper II**. The groups were defined as the follows: (I) single crystals, (II) particles with exclusively twin-boundaries, (III) particles with 2-3 grains separated by high-angle grain boundaries (HAGBs), (IV) particles with 4-6 grains separated by HAGBs and (V) particles with 7 or more grains separated by HAGBs.

### 6.3 DFSS *in situ* oxidation measurement

The Cu nanoparticles were fabricated by EBL to yield particles in a pre-determined pattern that enables easy recognition of the same particles in both TEM and DFSS measurements. The Cu particles were arranged in columns separated by 10  $\mu\text{m}$  with 7  $\mu\text{m}$  in between each row of particles, which is enough space to acquire the background scattering in between the particles, as explained in the previous chapter. The sample design, which is visualized in Figure 6.3 by a photograph of the scattered light of a sample collected through the dark-field objective, enables monitoring of multiple particles during one single measurement. With the current design, a maximum of 15 particles were probed simultaneously. The number is limited by a compromise between

the magnification in the microscope optical path and how many particle images that fit on the CCD chip.

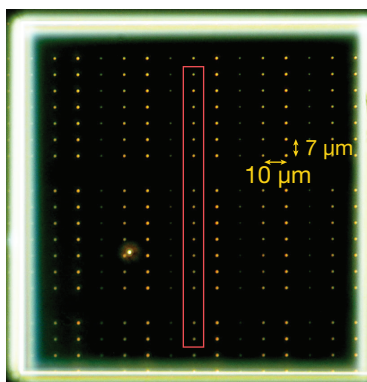


Figure 6.3: The sample design. An image of the sample collected through the dark-field objective, in which the smallest particle columns are barely distinguishable due to very weak scattering. The diameters of the disks are approximately 80, 100 and 120 nm, all with a height of 40 nm. The red box indicates the area from which the scattered light can be collected through the inlet slit of the spectrophotometer. The diffuse, bright square is scattering stemming from the tilted Si edges supporting the TEM membrane.

The scattering spectra of the 15 particles were collected for 10 minutes in pure Ar, preceding the O<sub>2</sub> interval, under which 1% O<sub>2</sub> was mixed with the Ar carrier gas. The length of the O<sub>2</sub> interval varied, depending on which end state I wanted to image in the TEM. However, the scattering signal was always collected for 10 minutes following the O<sub>2</sub> interval to validate that the oxidation had stopped and the optical read-out had stabilized. Usually, I observed a slight sample drift in both lateral and vertical direction during the kinetic measurements. This drift was significant in measurements that were longer than 30 minutes and it had to be corrected for manually by moving the sample stage in small increments. The drift is likely induced by a slow accumulation of heat in the objective, radiating from the heated reaction cell. Therefore, the final static spectra of the 15 particles were collected once again after the kinetic measurement, to ensure that the focus correction was done correctly.

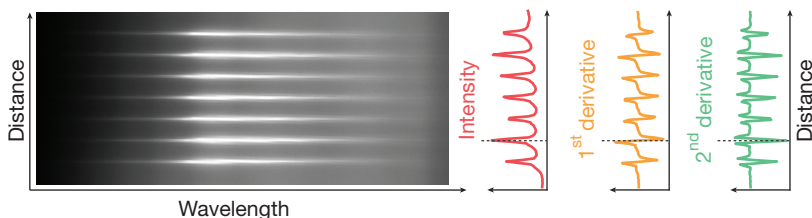


Figure 6.4: The principle of the particle-tracking algorithm. The centers of the particles are found by localizing the minima in the second derivative of the total intensity over all wavelengths at each vertical position (green plot). The position of the minima correspond to the same positions as the peaks in the total scattering intensity (red plot).

Image mode optical data acquisition enabled *post* measurement particle tracking during the data analysis (Figure 6.4) parallel to the spectrophotometer inlet slit. In other words, movement of the particles in the vertical direction on the CCD chip could be tracked and corrected for. Specifically, the centers of the particles were localized by finding the minima of the second derivative of the total intensity of all wavelengths for each position (on the y-axis) in the spectrum image. A peak in the intensity thus corresponds to an inflection point in the first derivative and a minimum in the second derivative, as depicted in Figure 6.4. Hence, the maximum intensity can be found by localizing the minima in the second derivative. A threshold value on the intensity was not used to find the particle center, due to the intensity variation over the TEM window originating from the strong scattering from the tilted edge of the Si substrate supporting the TEM window. This algorithm was then repeated every 10 data points in time, to enable the particle tracking.

As mentioned in the previous section, a polymerized hydrocarbon layer may be deposited on top of the particle during TEM imaging. To ensure that no such layer of a significant thickness was formed (since it would change the kinetics of the oxidation), the last optical spectrum taken after the oxidation for each particle was compared to the corresponding spectra of particles that had not been imaged during the pre-oxidation TEM step. When the precautions as described above were followed, i.e. initial annealing followed by immediate TEM imaging, no difference was observed in the spectra between these two particle populations, which I interpreted as TEM imaging not having influenced the oxidation kinetics.

## 6.4 Post-oxidation TEM imaging

The post-oxidation TEM imaging step, following the *in situ* DFSS measurements was carried out to observe the structural changes of the particles during the oxidation. From scrutinizing the structural changes, some insights into the oxidation mechanisms were obtained: (a) the Kirkendall void growth and its effect on the resonance scattering response as discussed in **paper I**, and (b) the dependence of the oxidation time on the initial grain structure of the reduced particles, as discussed in **paper II**. For a somewhat more comprehensive summary of the findings reported in these two papers, I refer to the next chapter. Anyhow, the post-oxidation TEM step is equally important as the pre-oxidation imaging. It provides information about the oxidation mechanisms, particularly by interrupting the oxidation progress at different time points. The imaging was performed exactly in the same manner as the pre-oxidation imaging, in a Tecnai T20 electron microscope.

## 6.5 Data analysis

Analysis of the images obtained from the pre- and post-oxidation imaging provided the means for calculating the oxide shell thickness and the volume oxidation fraction from the relation between the volume of the oxide shell and the metal core, which describes how far each individual particle had oxidized. In particular, the oxide shell thickness was calculated as the difference between the radius of the particle after annealing  $a_0$ , and

after partial oxidation  $a_2$ , extracted from the pre-oxidation and post-oxidation images respectively. This is correct, in the NKE limit where it is assumed that no core contraction occurs. By rewriting eq. (2.4) from chapter 2, the volume oxidation fraction  $\delta$  was calculated as

$$\delta = \frac{1}{Z} \left( \frac{a_2^3}{a_0^3} - 1 \right) \quad (6.1)$$

where  $Z$  is the bulk expansion coefficient. It tells how far oxidized each particle is at the point when the oxidation was interrupted.

# 7 SUMMARY AND OUTLOOK

My work is part of a project called *Single Particle Catalysis in Nanoreactors* and my contribution to this project lies in the characterization of the catalyst particles before, during and after the reaction. In this chapter, a summary of my findings during the first years of my graduate studies, condensed into two papers, is given, together with some ideas for further developing the correlative DFSS-TEM method and possible paths for widening the scope for its applications over the next couple of years.

## 7.1 Summary of the appended papers

In **paper I**, the correlative DFSS and TEM method for *in situ* Cu nanoparticle oxidation measurements is presented. In the paper, the scattering response of the single Cu particles collected *in situ* during oxidation is analyzed and qualitatively compared to a FDTD simulation model of the oxidation process. The specific finding reported in this paper is the characteristic spectral evolution detected during oxidation of Cu nanoparticles in the nanoscale Kirkendall effect (NKE) limit. A dramatic change of the scattering spectrum occurs when the oxidation mechanism changes from the initial oxide shell growth to the Kirkendall void formation and sequential growth. It was observed, that this transition happens after that approximately 30% of the initial metal volume has been converted into oxide, which agrees with earlier reports on ensemble measurements.<sup>13</sup> In the scattering spectrum, the onset of the Kirkendall void formation is reflected as a split of the LSPR mode into two modes, due to the increasing asymmetry of the remaining metal core when the void grows in size. By the chosen FDTD model, we could validate that the two modes appearing in the scattering spectrum indeed are due to the increase in aspect ratio of the metal core induced by the growing void.

The methods and findings established in **paper I**, were then further explored in **paper II**, where we analyze the dependence of the oxidation kinetics on the initial grain structure of the metal nanoparticles, using the onset of void formation signaled by the peak split in the single particle LSPR signal as the key descriptor. We define 5 grain structure groups for categorizing the nanoparticles from the pre-oxidation TEM images, depending on the number of grains they are comprised of. A trend of shorter time until peak split was observed for particles with higher grain number and high abundance of high-angle grain boundaries (HAGBs). Furthermore, we scrutinized the local origin of

the Kirkendall void formation and found proof that void nucleation is favored at areas with high density of HAGBs.

## 7.2 Outlook

I see a multitude of interesting possibilities for the development of my research work over the next couple of years. Firstly, the correlative DFSS-TEM method could be further improved by implementing a focus feedback loop<sup>79</sup> to overcome the issue of focus drift and lateral drift on the CCD chip due to heat accumulation in the objective. Such a feedback loop would enable reliable optical readout during longer measurements, which might be a requirement for pursuing some of the ideas of new areas presented below that could benefit from applying the correlative DFSS-TEM method.

The next step for developing the correlative method would be to implement transmission Kikuchi diffraction (TKD) with the help from our collaborators at DTU. As TKD is the natural pre-oxidation characterization method of the particle grain structure to perform not only a qualitative but also quantitative study of the grain structure effect on the oxidation time until Kirkendall void formation. As TKD, previously has been successfully used to analyze the grain structure of Pd nanoparticles yielding crystal grain orientations and grain boundary lengths.<sup>55</sup> However, including further steps in the measurement sequence induces more practical issues, such as hydrocarbon polymerization by the electron beam, which protects Cu nanoparticles from oxidizing, as first tests in this direction have shown. Hopefully, in the near future a practical solution can be found to introduce TKD for the pre-oxidation characterization.

Apart from improving the method, widening the scope to study other materials would possibly provide many interesting questions to explore in the future. Here, plasmonic alloy nanoparticles could be an interesting candidate, since within our group there are activities to use such alloy materials for both sensing and photocatalysis. However, some fundamental understanding of the alloying process is lacking, which could perhaps benefit from correlative single particle DFSS-TEM studies. Following the plasmonic signal *in situ* during alloying might shed some light on the changes the particle undergoes in the alloying process. The *in situ* DFSS measurements would, in the same way as in the case of Cu oxidation, be correlated to TEM images, as well as elementary analysis by energy-dispersive X-ray spectroscopy (EDS) of the particle pre- and post-alloying.

A second natural path for the further application of the correlative method would be to implement *in situ* plasmonic spectroscopy to track the oxidation state of the Cu nanoparticles during heterogeneous catalysis. One reaction to study could be the oxidation of CO, since Cu is an active catalyst for this reaction. This path aligns well with the scope of the project and could be the link between my work and the nanoreactor activities within the project.

In addition to these ideas for the future applications of the correlative DFSS-TEM method, I also hope to continue the work on *in situ* TEM Cu nanoparticle oxidation together with our collaborators at DTU. There, we combine the *in situ* TEM with EELS

to better understand the fundamental mechanisms during Cu nanoparticle oxidation and how it affects the plasmonic resonance of the particle.



# ACKNOWLEDGEMENTS

First of all I want to acknowledge the financial support to the project I am part of, the Knut and Alice Wallenberg Foundation project 2015.0055 and the financial support to the MC2 cleanroom by the Knut and Alice Wallenberg foundation.

There are so many people I want to thank for supporting me to achieve this thesis, here are some that deserve extra acknowledgement.

Most of all, thanks to Christoph for giving me this opportunity and believing that I can achieve this, and further things in the future. Thank you for all the support, guidance and all the great ideas!

Thanks also to my co-supervisors, Fredrik Westerlund and Anders Hellman, and to my examiner Henrik Grönbeck for the feedback on this thesis.

Thanks to everyone in the KAW project, it is really interesting to be part of such an interdisciplinary project.

I want to thank the MC2 cleanroom and the CMAL personnel, a special thanks to Stefan Gustafsson, for teaching me everything about the TEMs.

Thanks to all present and former members of Chemical Physics, for being such great colleges and for all the fun conversations in the lunch room. In particular, to the people in the Langhammer group for being such a great group to be a part of.

A special thanks to Joachim and David for helping with the nanofabrication. As well as to David, for all your great ideas and inputs, and for bringing me on the skiing conferences. ☺

Thanks to Tomasz, for teaching me everything I know about FDTD.

Shima, Alice, Monia and Jakob at DTU, I really appreciate all the time you put into our collaborations, we have something great going on and I think it is going to be really interesting to see the results that will come out of it.

As customary last, but definitely not least, thanks to my friends, for making me enjoy other things in life than research. To my family, for always supporting me in life, no matter what choices I make. And to Erik, for supporting me, putting up with all my work and for making this year the best ever! I love you!



# BIBLIOGRAPHY

1. Twigg, M. V. & Spencer, M. S. Deactivation of Copper Metal Catalysts for Methanol Decomposition, Methanol Steam Reforming and Methanol Synthesis. *Top. Catal.* **22**, 191–203 (2003).
2. Rihko-Struckmann, L. K., Peschel, A., Hanke-Rauschenbach, R. & Sundmacher, K. Assessment of Methanol Synthesis Utilizing Exhaust CO<sub>2</sub> for Chemical Storage of Electrical Energy. *Ind. Eng. Chem. Res.* **49**, 11073–11078 (2010).
3. Dry, M. E. The Fischer–Tropsch process: 1950–2000. *Catal. Today* **71**, 227–241 (2002).
4. Pérez-Fortes, M., Schöneberger, J. C., Boulamanti, A. & Tzimas, E. Methanol synthesis using captured CO<sub>2</sub> as raw material: Techno-economic and environmental assessment. *Appl. Energy* **161**, 718–732 (2016).
5. Song, J. *et al.* Corrosion Protection of Electrically Conductive Surfaces. *Metals (Basel)*. **2**, 450–477 (2012).
6. Williams, D. B. & Carter, C. B. in *Transmission Electron Microscopy* 3–17 (Springer US, 1996). doi:10.1007/978-1-4757-2519-3\_1
7. Mayer, K. M. & Hafner, J. H. Localized Surface Plasmon Resonance Sensors. *Chem. Rev.* **111**, 3828–3857 (2011).
8. Bingham, J. M., Anker, J. N., Kreno, L. E. & Van Duyne, R. P. Gas Sensing with High-Resolution Localized Surface Plasmon Resonance Spectroscopy. *J. Am. Chem. Soc.* **132**, 17358–17359 (2010).
9. Larsson, E. M., Syrenova, S. & Langhammer, C. Nanoplasmonic sensing for nanomaterials science. *Nanophotonics* **1**, 249–266 (2012).
10. Nugroho, F. A. A., Eklund, R., Nilsson, S. & Langhammer, C. A fiber-optic nanoplasmonic hydrogen sensor *via* pattern-transfer of nanofabricated PdAu alloy nanostructures. *Nanoscale* **10**, 20533–20539 (2018).
11. Albinsson, D., Nilsson, S., Antosiewicz, T. J., Zhdanov, V. P. & Langhammer, C. Heterodimers for in Situ Plasmonic Spectroscopy: Cu Nanoparticle Oxidation Kinetics, Kirkendall Effect, and Compensation in the Arrhenius Parameters. *J. Phys. Chem. C* **123**, 6284–6293 (2019).

12. Rice, K. P., Paterson, A. S. & Stoykovich, M. P. Nanoscale Kirkendall Effect and Oxidation Kinetics in Copper Nanocrystals Characterized by Real-Time, In Situ Optical Spectroscopy. *Part. Part. Syst. Charact.* **32**, 373–380 (2015).
13. Susman, M. D., Feldman, Y., Bendikov, T. A., Vaskevich, A. & Rubinstein, I. Real-time plasmon spectroscopy study of the solid-state oxidation and Kirkendall void formation in copper nanoparticles. *Nanoscale* **9**, 12573–12589 (2017).
14. Qin, L. X., Jing, C., Li, Y., Li, D. W. & Long, Y. T. Real-time monitoring of the aging of single plasmonic copper nanoparticles. *Chem. Commun.* (2012). doi:10.1039/c1cc14326c
15. Huang, C.-L., Weng, W.-L., Liao, C.-N. & Tu, K. N. Suppression of interdiffusion-induced voiding in oxidation of copper nanowires with twin-modified surface. *Nat. Commun.* **9**, 340 (2018).
16. Tokozakura, D., Nakamura, R., Nakajima, H., Lee, J.-G. & Mori, H. Transmission electron microscopy observation of oxide layer growth on Cu nanoparticles and formation process of hollow oxide particles. *J. Mater. Res.* **22**, 2930–2935 (2007).
17. LaGrow, A. P., Ward, M. R., Lloyd, D. C., Gai, P. L. & Boyes, E. D. Visualizing the Cu/Cu<sub>2</sub>O Interface Transition in Nanoparticles with Environmental Scanning Transmission Electron Microscopy. *J. Am. Chem. Soc.* **139**, 179–185 (2017).
18. He, X. *et al.* Controllable in Situ Surface Restructuring of Cu Catalysts and Remarkable Enhancement of Their Catalytic Activity. *ACS Catal.* **9**, 2213–2221 (2019).
19. El Mel, A.-A. *et al.* Electron Beam Nanosculpting of Kirkendall Oxide Nanochannels. *ACS Nano* **8**, 1854–1861 (2014).
20. Leidheiser, H. & Musić, S. The atmospheric corrosion of iron as studied by Mössbauer spectroscopy. *Corros. Sci.* **22**, 1089–1096 (1982).
21. FitzGerald, K. P., Nairn, J., Skennerton, G. & Atrens, A. Atmospheric corrosion of copper and the colour, structure and composition of natural patinas on copper. *Corros. Sci.* **48**, 2480–2509 (2006).
22. Tuck, C. D. S., Powell, C. A. & Nuttall, J. 3.07 - Corrosion of Copper and its Alloys. *Shreir's Corros.* **3**, 1937–1973 (2010).
23. Gawande, M. B. *et al.* Cu and Cu-Based Nanoparticles: Synthesis and Applications in Catalysis. *Chem. Rev.* **116**, 3722–3811 (2016).

24. Kasap, S., Koughia, C. & Ruda, H. E. in *Springer Handbook of Electronic and Photonic Materials* (Springer International Publishing, 2017). doi:10.1007/978-3-319-48933-9\_2
25. Ross, J. in *Heterogeneous catalysis: fundamentals and applications* (Elsevier, 2012).
26. Lide, D. R. in *CRC Handbook of Chemistry and Physics* (CRC Press, Boca Raton, FL, 2005).
27. Chorkendorff, I. & Niemantsverdriet, J. W. *Concepts of Modern Catalysis and Kinetics*. (Wiley-VCH Verlag GmbH & Co. KGaA, 2003). doi:10.1002/3527602658
28. Hauffe, K. *Oxidation of Metals*. (Springer US, 1995). doi:10.1007/978-1-4684-8920-0
29. Cabrera, N. & Mott, N. F. Theory of the Oxidation of Metals. *Rep. Prog. Phys.* **12**, (1949).
30. Anderson, B. D. & Tracy, J. B. Nanoparticle conversion chemistry: Kirkendall effect, galvanic exchange, and anion exchange. *Nanoscale* **6**, (2014).
31. Carter, R. E. Kinetic Model for Solid-State Reactions. *J. Chem. Phys.* **34**, 2010–2015 (1961).
32. Susman, M. D., Vaskevich, A. & Rubinstein, I. A General Kinetic-Optical Model for Solid-State Reactions Involving the Nano Kirkendall Effect. The Case of Copper Nanoparticle Oxidation. *J. Phys. Chem. C* **120**, 16140–16152 (2016).
33. Railsback, J. G., Johnston-Peck, A. C., Wang, J. & Tracy, J. B. Size-Dependent Nanoscale Kirkendall Effect During the Oxidation of Nickel Nanoparticles. *ACS Nano* **4**, 1913–1920 (2010).
34. Nakamura, R., Tokozakura, D., Nakajima, H., Lee, J.-G. & Mori, H. Hollow oxide formation by oxidation of Al and Cu nanoparticles. *J. Appl. Phys.* **101**, 074303 (2007).
35. Fan, H. J., Gösele, U. & Zacharias, M. Formation of Nanotubes and Hollow Nanoparticles Based on Kirkendall and Diffusion Processes: A Review. *Small* **3**, 1660–1671 (2007).
36. El Mel, A. A., Nakamura, R. & Bittencourt, C. The Kirkendall effect and nanoscience: Hollow nanospheres and nanotubes. *Beilstein Journal of Nanotechnology* **6**, (2015).
37. Freestone, I., Meeks, N., Sax, M. & Higgitt, C. The Lycurgus Cup — A Roman

- nanotechnology. *Gold Bull.* **40**, 270–277 (2007).
38. The British Museum. Available at: [www.britishmuseum.org](http://www.britishmuseum.org). (Accessed: 21st March 2019)
  39. Kreibig, U. & Vollmer, M. *Optical properties of metal clusters*. (Springer, 1995).
  40. Maier, S. A. *Plasmonics: Fundamentals and Applications*. (Springer US, 2007). doi:10.1007/0-387-37825-1
  41. Bohren, C. F. & Huffman, D. R. *Absorption and Scattering of Light by Small Particles*. (Wiley-VCH Verlag GmbH, 1998). doi:10.1002/9783527618156
  42. Mock, J. J., Barbic, M., Smith, D. R., Schultz, D. A. & Schultz, S. Shape effects in plasmon resonance of individual colloidal silver nanoparticles. *J. Chem. Phys.* **116**, 6755–6759 (2002).
  43. Bryant, G. W., Abajo, F. J. G. de & Aizpurua, J. Mapping the Plasmon Resonances of Metallic Nanoantennas. *Nano Lett.* **8**, 631–636 (2008).
  44. Kane Yee. Numerical solution of initial boundary value problems involving maxwell's equations in isotropic media. *IEEE Trans. Antennas Propag.* **14**, 302–307 (1966).
  45. Zhao, J. *et al.* Methods for Describing the Electromagnetic Properties of Silver and Gold Nanoparticles. *Acc. Chem. Res.* **41**, 1710–1720 (2008).
  46. George H. Chan, Jing Zhao, Erin M. Hicks, Schatz, G. C. & Duynes, R. P. Van. Plasmonic Properties of Copper Nanoparticles Fabricated by Nanosphere Lithography. *Nano Lett.* **7**, 1947–1952 (2007).
  47. Langhammer, C., Yuan, Z., Zorić, I. & Kasemo, B. Plasmonic Properties of Supported Pt and Pd Nanostructures. *Nano Lett.* **6**, 833–838 (2006).
  48. Langhammer, C., Schwind, M., Kasemo, B. & Zorić, I. Localized Surface Plasmon Resonances in Aluminum Nanodisks. *Nano Lett.* **8**, 1461–1471 (2008).
  49. Langhammer, C., Zorić, I., Kasemo, B. & Clemens, B. M. Hydrogen Storage in Pd Nanodisks Characterized with a Novel Nanoplasmonic Sensing Scheme. *Nano Lett.* **7**, 3122–3127 (2007).
  50. Wadell, C. *et al.* Hysteresis-Free Nanoplasmonic Pd–Au Alloy Hydrogen Sensors. *Nano Lett.* **15**, 3563–3570 (2015).
  51. Nugroho, F. A. A., Darmadi, I., Zhdanov, V. P. & Langhammer, C. Universal Scaling and Design Rules of Hydrogen-Induced Optical Properties in Pd and Pd-Alloy Nanoparticles. *ACS Nano* **12**, 9903–9912 (2018).

52. Nugroho, F. A. A., Iandolo, B., Wagner, J. B. & Langhammer, C. Bottom-Up Nanofabrication of Supported Noble Metal Alloy Nanoparticle Arrays for Plasmonics. *ACS Nano* **10**, 2871–2879 (2016).
53. Bu, Y., Niemantsverdriet, J. W. H. & Fredriksson, H. O. A. Cu Model Catalyst Dynamics and CO Oxidation Kinetics Studied by Simultaneous in Situ UV-Vis and Mass Spectroscopy. *ACS Catal.* **6**, 2867–2876 (2016).
54. Syrenova, S. *et al.* Hydride formation thermodynamics and hysteresis in individual Pd nanocrystals with different size and shape. *Nat. Mater.* **14**, 1236–1244 (2015).
55. Alekseeva, S. *et al.* Grain boundary mediated hydriding phase transformations in individual polycrystalline metal nanoparticles. *Nat. Commun.* **8**, 1084 (2017).
56. Boyer, D., Tamarat, P., Maali, A., Lounis, B. & Orrit, M. Photothermal Imaging of Nanometer-Sized Metal Particles Among Scatterers. *Science* **297**, 1160–1163 (2002).
57. Kumar, C. S. S. R. (Challa S. S. R. . *Raman spectroscopy for nanomaterials characterization*. (Springer, 2012).
58. Hecht, B. *et al.* Scanning near-field optical microscopy with aperture probes: Fundamentals and applications. *J. Chem. Phys.* **112**, 7761–7774 (2000).
59. Nelayah, J. *et al.* Mapping surface plasmons on a single metallic nanoparticle. *Nat. Phys.* **3**, 348–353 (2007).
60. Gómez-Medina, R., Yamamoto, N., Nakano, M. & García de Abajo, F. J. Mapping plasmons in nanoantennas via cathodoluminescence. *New J. Phys.* **10**, 105009 (2008).
61. Brock, D. C. & Moore, G. E. in *Understanding Moore's law : four decades of innovation* 122 (Chemical Heritage Foundation, 2006).
62. Feynman, R. P. There's plenty of room at the bottom [data storage]. *J. Microelectromechanical Syst.* **1**, 60–66 (1992).
63. Lambert, L. & Mulvey, T. Ernst Ruska (1906–1988), Designer Extraordinaire of the Electron Microscope: A Memoir. *Adv. Imaging Electron Phys.* **95**, 2–62 (1996).
64. Wang, Z., Ai, B., Möhwald, H. & Zhang, G. Colloidal Lithography Meets Plasmonic Nanochemistry. *Adv. Opt. Mater.* **6**, 1800402 (2018).
65. Fredriksson, H. *et al.* Hole–Mask Colloidal Lithography. *Adv. Mater.* **19**, 4297–4302 (2007).

66. Syrenova, S., Wadell, C. & Langhammer, C. Shrinking-Hole Colloidal Lithography: Self-Aligned Nanofabrication of Complex Plasmonic Nanoantennas. *Nano Lett.* **14**, 2655–2663 (2014).
67. Cheng, X. Nanostructures: fabrication and applications. *Nanolithography* 348–375 (2014). doi:10.1533/9780857098757.348
68. Li, K. *et al.* High speed e-beam writing for large area photonic nanostructures — a choice of parameters. *Sci. Rep.* **6**, 32945 (2016).
69. Nguyen, N.-T. & Nguyen, N.-T. Fabrication technologies. *Micromixers* 113–161 (2012). doi:10.1016/B978-1-4377-3520-8.00004-8
70. Lentzen, M. *et al.* High-resolution imaging with an aberration-corrected transmission electron microscope. *Ultramicroscopy* **92**, 233–242 (2002).
71. Olson, J. *et al.* Optical characterization of single plasmonic nanoparticles. *Chem. Soc. Rev.* **44**, 40–57 (2015).
72. Egerton, R. F. *Physical Principles of Electron Microscopy*. (Springer International Publishing, 2016). doi:10.1007/978-3-319-39877-8
73. Grant, A. W., Hu, Q.-H. & Kasemo, B. Transmission electron microscopy windows for nanofabricated structures. *Nanotechnology* **15**, 1175–1181 (2004).
74. Kohl, H. & Reimer, L. *Transmission Electron Microscopy*. **36**, (Springer New York, 2008).
75. Vendelbo, S. B. *et al.* Visualization of oscillatory behaviour of Pt nanoparticles catalysing CO oxidation. *Nat. Mater.* **13**, 884–890 (2014).
76. Egerton, R. F., Li, P. & Malac, M. Radiation damage in the TEM and SEM. *Micron* **35**, 399–409 (2004).
77. Li, J. & Liu, C. Carbon-coated copper nanoparticles: synthesis, characterization and optical properties. *New J. Chem.* **33**, 1474 (2009).
78. Yang, L., Yan, B. & Reinhard, B. M. Correlated Optical Spectroscopy and Transmission Electron Microscopy of Individual Hollow Nanoparticles and their Dimers. *J. Phys. Chem. C* **112**, 15989–15996 (2008).
79. Aćimović, S. S. *et al.* Antibody–Antigen Interaction Dynamics Revealed by Analysis of Single-Molecule Equilibrium Fluctuations on Individual Plasmonic Nanoparticle Biosensors. *ACS Nano* **12**, 9958–9965 (2018).